

# A high resolution view of tropical shallow clouds

Master's Thesis

Theresa Mieslinger  
June 18, 2017

Supervisors: Prof. Dr. Stefan A. Bühler  
Dr. Ákos Horváth

Institution: Meteorologisches Institut  
Universität Hamburg

Master's thesis on the topic:  
A high resolution view of tropical shallow clouds

## Abstract

This study on cloud field properties investigates shallow cumulus clouds over tropical oceans by analyzing 1917 high-resolution ASTER images recorded between 2000 and 2007. Clouds are characterized by the cloud size distribution and the fractal dimension, which relates cloud area to cloud perimeter. Cloud fraction and cloud top height are calculated for each ASTER granule and the cloud spatial distribution is characterized by nearest neighbor statistics and the simple convective aggregation index (SCAI). In general, the calculated cloud field properties are in good agreement with findings from previous studies. The average cloud fraction is 11.8 %, with clouds exhibiting an average cloud top height of 1.2 km. Assuming a single power law, a slope of -2.85 is found for a fit to the cloud size distribution, while a scale break size at 600 m characterizes a double power law fit. A fractal dimension of 1.21 is found and the analysis of the spatial distribution shows that cloud fields are more frequently in an aggregated state. Relating cloud field properties to the large-scale meteorological state indicates a strong influence of wind speed on cloud development and cloud organization. With increasing wind speed, the trade wind layer deepens and clouds are observed to be larger, deeper, and more numerous. Consequently, the cloud fraction increases. The influence of column water vapor on cloud field properties is more ambiguous. The analysis indicates larger clouds to develop in very moist and very dry situations, which are most likely linked to different processes. Strong large-scale subsidence and a stable lower troposphere, on the other hand, are clearly related to larger clouds and a higher cloud fraction.

# Contents

<b>1. Introduction</b>	<b>7</b>
<b>2. Shallow cumulus clouds and the trade wind layer</b>	<b>9</b>
<b>3. Data</b>	<b>10</b>
3.1. ASTER instrument data . . . . .	10
3.1.1. Data specification . . . . .	10
3.1.2. Conversion to physical units . . . . .	11
3.1.3. ASTER sample image . . . . .	13
3.2. MODIS cloud products . . . . .	14
3.3. ERA-Interim reanalysis data . . . . .	15
<b>4. Methodology</b>	<b>18</b>
4.1. ASTER scene selection . . . . .	18
4.2. ASTER cloud mask . . . . .	19
4.3. Validation of the ASTER cloud mask . . . . .	22
4.4. Cloud labeling method . . . . .	25
<b>5. Cloud field properties from ASTER images</b>	<b>26</b>
5.1. Cloud fraction . . . . .	26
5.2. Cloud top height . . . . .	26
5.3. Cloud shape . . . . .	28
5.3.1. Cloud size distribution . . . . .	29
5.3.2. Fractal dimension . . . . .	33
5.4. Spatial distribution . . . . .	35
5.4.1. Nearest neighbor analysis . . . . .	36
5.4.2. Simple Convective Aggregation Index . . . . .	37
<b>6. Physical parameters controlling cloud field properties</b>	<b>39</b>
6.1. Moisture in the lower troposphere . . . . .	39
6.2. The trade wind boundary layer height . . . . .	43
6.3. Additional parameters . . . . .	47
6.3.1. Wind shear . . . . .	47
6.3.2. Vertical velocity . . . . .	48
6.3.3. Lower tropospheric stability . . . . .	52
6.4. Cloud feedback in a warming climate . . . . .	54
<b>7. Limitations of the study</b>	<b>56</b>
<b>8. Conclusions and outlook</b>	<b>58</b>
<b>A. Appendix A</b>	<b>61</b>
A.1. Cloud mask . . . . .	61

A.2. Cloud properties . . . . .	63
A.3. TCWV from ERA-interim . . . . .	63
<b>Acronyms</b>	<b>65</b>
<b>References</b>	<b>66</b>
<b>Versicherung an Eides statt</b>	<b>72</b>



# 1. Introduction

Shallow cumulus clouds are a typical feature above warm ocean surfaces in trade wind regions around the globe. Clouds interact with the circulation through phase change, turbulent transport and by influencing radiative transfer [Bony et al., 2015]. Trade wind cumuli contribute a substantial part to the global cloud coverage. Due to their high albedo and low altitude they have a cooling effect on the atmosphere. The behavior of this cloud type in a changing climate has become increasingly important because of its relevance to the global climate and it is subject of several recent studies (Nuijens et al. [2014], Brient et al. [2015], Bretherton [2015]). Climate models exhibit a large spread in assessing how shallow cumulus cloud fields react to warming. This demonstrates the ignorance of the underlying physical processes as well as the interaction with large-scale dynamics [Bony et al., 2015].

Increasing computational power offers the possibility of highly resolved simulations and an improved representation of shallow convection in climate models. However, observations are essential for validating model results. Over ocean, observations are scarcely available. Measurement campaigns like Rain In Cumulus over the Ocean (RICO) and the two Next-Generation Airborne Remote Sensing for Validation Studies (NARVAL) campaigns, NARVAL-I and just recently NARVAL-II, are dedicated to gain a better understanding of physical and dynamical processes in the trade wind boundary layer.

One major weakness of such campaigns is that the acquired information is limited in space and time. Observational sites like the Barbados Cloud Observatory (BCO) provide long-term measurements but again, the information is site specific. Satellite observations help to overcome these sampling limitations by providing long-term datasets that cover large parts of the Earth. The coarse spatial resolution of satellite images usually restricts studies to clouds with a horizontal extent larger than 1 km. This excludes trade wind cumuli, the vast majority of which has sizes of less than 2 km [Zhao and Di Girolamo, 2007].

The Advanced Spaceborne Thermal Emission and Reflection Radiometer (ASTER) instrument on Terra is particularly well suited for a study of such small clouds due to its unique high resolution of up to 15 m in the short wave bands. Originally, ASTER was not designed for cloud observations, which leads to some sampling limitations discussed later on. Zhao and Di Girolamo [2007] used 152 ASTER images recorded during the RICO campaign to investigate macrophysical properties of trade wind cumuli observed near Barbados. Since April 2016, the complete ASTER data archive has been freely accessible allowing for a more comprehensive study.

The aim of the current work is the creation and analysis of a large dataset suited to investigate shallow cumulus clouds in the trades. The potential of the ASTER instrument for analyzing small cumulus clouds is evaluated on the basis of a larger

dataset compared to previous studies. Moreover, cloud field properties are calculated from the new dataset. Parameters such as cloud fraction (Wood and Bretherton [2006], Brueck et al. [2015]), cloud size distribution (Benner et al. [1998], Neggers et al. [2003], Trivej and Stevens [2010]) and spatial distribution (Benner et al. [1998], Lonitz [2014]), as well as the cloud depth (Genkova et al. [2007], Nuijens and Stevens [2012]) are commonly used to describe cloud fields and are also considered in this study. Subsequently, the information of cloud properties gathered from ASTER images is combined with water vapor data from the Moderate-resolution Imaging Spectroradiometer (MODIS) and large-scale meteorological parameters from the ECMWF ERA-interim reanalysis to provide further insight into cloud development and cloud organization.

Such an analysis is by no means new, but previous studies used either data with a much coarser resolution, e.g. from MODIS in Brueck et al. [2015], or they are based on only a few cases (see Table 1 in Zhao and Di Girolamo [2007]). Using a one to two orders of magnitude larger dataset ensures a more robust statistic and enables the investigation of relations between cloud field properties and meteorological variables.

This work starts with a short introduction to known characteristics of shallow cumulus clouds and the trade wind boundary layer in Chapter 2. Chapter 3 describes the ASTER data as well as supplementary data from MODIS and ERA-interim. Chapter 4 illustrates the data set selection and the implementation of a sophisticated cloud mask. This is an important step, because all further calculations depend on the quality of the cloud mask. In Chapter 5, the derivation of cloud field properties is described and results from the ASTER dataset are shown. Chapter 6 summarizes relations of cloud field properties to meteorological conditions, such as the amount of water vapor and the trade wind boundary layer height, as observed in the analyzed images.

## 2. Shallow cumulus clouds and the trade wind layer

Shallow cumulus clouds are a characteristic feature of the thermal boundary layer in the trade wind regions. In the literature they are variously referred to as tropical shallow cumulus, trade wind cumulus or popcorn cumulus clouds. The trade wind regions owe their name to the strong easterly winds that are part of the Hadley circulation. They are located north and south of the equator where air masses rising within the Inter-Tropical-Convergence Zone (ITCZ) start to cool and sink down again.

Trade wind cumuli are prevalent in those regions with mean subsiding motion. In the northern hemisphere, such conditions are typically observed during boreal winter months over the western parts of the ocean basins. However, during the wet summer season shallow cumulus clouds can also be observed despite moderate rising motion. In this case, they are typically found in between deep convective clouds [Brueck et al., 2015].

The trade wind boundary layer is typically composed of a well-mixed subcloud layer above the surface, followed by a transition layer and the cloud base at about 700 m. The cloud layer spans from the transition layer up to the capping inversion, usually found at a height of 1.5 km to 3 km and separating the moist and thermally unstable trade wind layer from the warm and dry lower free troposphere [Stevens et al., 2017]. A vertical cross-section of the layers is shown in Figure 1 including the terminology used throughout this work.

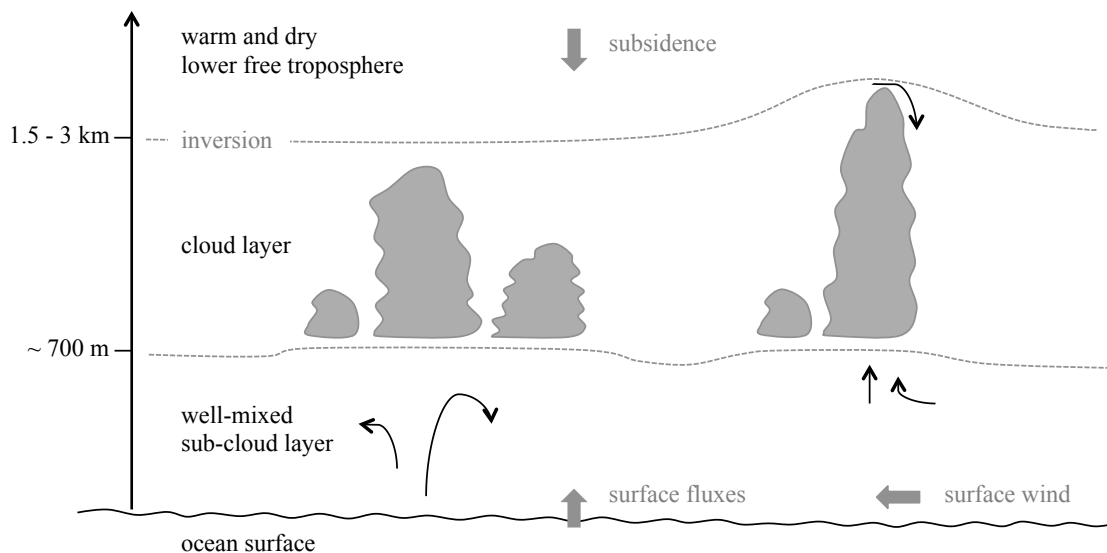


**Figure 1:** Vertical cross-section of a typical trade wind boundary layer including the layer names and the main physical and dynamical processes (adapted from Stevens [2005]).

## 3. Data

Since April 2016 ASTER images are available free of charge to the scientific community. The high spatial resolution, especially in the short wave bands, makes this dataset unique and well suited to study shallow cumulus clouds in the trades.

This chapter introduces the ASTER instrument and the data characteristics, followed by a short introduction to the data processing. Raw instrument data need to be converted to physical units. In addition, ASTER images are supplemented with data from MODIS and the global atmospheric European reanalysis dataset (ERA-interim). These datasets provide additional information on the large-scale meteorological conditions under which shallow cumulus clouds form. A brief description of the two supplementary data products and their usage is given.

### 3.1. ASTER instrument data

ASTER is a multispectral, dual-angle, high-resolution imager built by the Japanese Government and operated by a joint ASTER Science Team consisting of Japanese, Australian and American scientists. ASTER flies aboard the Terra research satellite, which is part of the National Aeronautics and Space Administration's (NASA) Earth Observing System and was launched in 1999. Terra is a polar-orbiting satellite in a sun-synchronous orbit at 705 km altitude, with an equator crossing time of 10:30 am local solar time.

The ASTER instrument was primarily designed for land emission and temperature studies, monitoring of volcanic activities, and for the construction of a high resolution digital elevation model of the Earth's surface.

#### 3.1.1. Data specification

ASTER consists of three separate radiometers measuring in different spectral regions. The visible and near-infrared (VNIR) sensors cover the range from  $0.53 \mu\text{m}$  to  $0.86 \mu\text{m}$  in three bands with 15 m spatial resolution. An additional telescope pointing backwards in the along-track direction at an angle of  $27.6^\circ$  and covering the same frequencies as band 3 allows for stereoscopic analysis. The radiometer in the shortwave infrared (SWIR) range consists of six bands in the range of  $1.60 - 2.43 \mu\text{m}$  at 30 m resolution and the thermal infrared (TIR) radiometer comprises five bands covering  $8.125 - 11.65 \mu\text{m}$  with 90 m spatial resolution [Yamaguchi et al., 1998].

The ASTER swath width is 60 km and the track is cut into  $60 \times 60 \text{ km}^2$  pieces, representing 9 seconds of observation time. The data acquisition is limited through the on-board storage space to about 310 scenes per day of Level 1B data. The Level 1B data is available as digital numbers representing calibrated radiance at

**Table 1:** ASTER sensor specifications. List of frequency bands with corresponding spectral ranges  $\Delta\lambda$ , as well as the unit conversion coefficients (UCC) for high, normal, low1, and low2 gain settings for the three radiometers respectively.

Radiometer (res.)	Band	$\Delta\lambda$ [ $\mu\text{m}$ ]	UCC [ $W/(m^2\text{sr}\mu\text{m})$ ]			
			high	normal	low1	low2
VNIR (15 m)	1	0.52 - 0.60	0.676	1.688	2.25	-
	2	0.63 - 0.69	0.708	1.415	1.89	-
	3N	0.76 - 0.86	0.423	0.862	1.15	-
	3B	0.76 - 0.86	0.423	0.862	1.15	-
SWIR (30 m)	4	0.160 - 1.70	0.1087	0.2174	0.290	0.290
	5	2.145 - 2.185	0.0348	0.0696	0.0925	0.409
	6	2.185 - 2.225	0.0313	0.0625	0.0830	0.390
	7	2.235 - 2.285	0.0299	0.0597	0.0795	0.332
	8	2.295 - 2.365	0.0209	0.0417	0.0556	0.245
	9	2.360 - 2.430	0.0159	0.0318	0.0424	0.265
	TIR (90 m)	10	8.125 - 8.475	-	0.006822	-
11		8.475 - 8.825	-	0.006780	-	-
12		8.925 - 9.275	-	0.006590	-	-
13		10.25 - 10.95	-	0.005693	-	-
14		10.95 - 11.65	-	0.005225	-	-

the sensor. In addition, geometric coefficients are included to get the proper map projection. Higher level data products are of minor quality (see Chapter 4.2). Further instrument details and information on the different datasets can be found in the ASTER handbook [M. Abrams and Ramachandran, 2002] and in Yamaguchi et al. [1998]. A list of all ASTER bands and corresponding wavelength regions can be found in Table 1.

The ASTER mission design prioritizes clear-sky land observations, which results in the relatively scarce availability of images containing clouds in general and especially over ocean. Therefore, this study is limited by the opportunistic acquisition of cloudy images. Still, thousands of images from the ASTER data archive can be used for cloud research. A detailed description of the selection of cloudy ASTER images follows in Chapter 4.1.

### 3.1.2. Conversion to physical units

Clouds can be observed from space due to two main features: In the short wave range the reflected solar light can be detected at the spacecraft. In thermal infrared bands clouds stand out because their cold top temperatures contrast with warmer surface pixels. The re-calibrated digital numbers,  $DN$ s, from all ASTER images are converted to reflectances in the VNIR and SWIR bands and to brightness

temperatures in the TIR range. In the first step, all images are converted to spectral radiances  $L_\lambda$  at the top of atmosphere (TOA) by multiplying  $DN$  with the band specific unit conversion coefficient (UCC) according to M. Abrams and Ramachandran [2002] :

$$L_\lambda = (DN - 1) \cdot UCC_\lambda, \quad (3.1)$$

where  $UCC_\lambda$  has the unit  $[W/m^2sr\mu m]$  and depends on the gain settings of the instrument, which are noted in the metadata of each ASTER data granule. All coefficients are taken from the ASTER handbook [M. Abrams and Ramachandran, 2002] and listed in Table 1.

In the next step, data recorded in the VNIR and SWIR bands are converted to spectral reflectances  $r_{\lambda, \Theta_z}$  at TOA:

$$r_{\lambda, \Theta_z} = \frac{\pi \cdot L_\lambda \cdot d_{SE}^2}{E_{SUN, \lambda} \cdot \cos(\Theta_z)}, \quad (3.2)$$

with  $r_\lambda$  reflectance at the effective band wavelength  $\lambda$   
 $d_{SE}$  Sun-Earth distance in astronomical units  
 $E_{SUN, \lambda}$  mean solar exoatmospheric irradiance in  $[\frac{W}{m^2\mu m}]$   
 $\Theta_z$  solar zenith angle in degree

$d_{SE}$  and  $\Theta_z$  can be calculated from the Sun-Earth geometry and the date.  $E_{SUN, \lambda}$  is obtained from the convolution of the ASTER band specific spectral response function with the extraterrestrial solar spectral irradiance, which is stated in Thome et al. [2001].

From the five thermal-infrared bands spectral radiance values are converted to brightness temperatures  $T_b$ . The conversion is based on the Planck function. Equation 3.3 is a rearranged version of the inverse Planck function and is used to calculate  $T_b$  depending on  $L_\lambda$  and on the wavelength dependent constants  $K_{1, \lambda}$  in  $[W/m^2sr\mu m]$  and  $K_{2, \lambda}$  in  $[K]$ .

$$T_b = \frac{K_{2, \lambda}}{\ln(\frac{K_{1, \lambda}}{L_\lambda} + 1)} \quad (3.3)$$

Values for  $E_{SUN, \lambda}$ ,  $K_{1, \lambda}$ , and  $K_{2, \lambda}$  are listed in Table 2.

**Table 2:** List of ASTER bands, their spectral range  $\Delta\lambda$ , and the corresponding solar spectral irradiance  $E_{SUN,\lambda}$  from Thome et al. [2001].  $K_{1,\lambda}$  and  $K_{2,\lambda}$  are wavelength-dependent calibration coefficients needed for calculating the brightness temperature (see Equation 3.3).

radiometer	Band	$\Delta\lambda$ [ $\mu m$ ]	$E_{SUN,\lambda}$ [ $W/(m^2\mu m)$ ]	$K_{1,\lambda}$ [ $W/(m^2sr\mu m)$ ]	$K_{2,\lambda}$ [K]
VNIR	1	0.52 - 0.60	1848	-	-
	2	0.63 - 0.69	1549	-	-
	3N	0.76 - 0.86	1114	-	-
	3B	0.76 - 0.86	-	-	-
SWIR	4	0.160 - 1.70	225.4	-	-
	5	2.145 - 2.185	86.63	-	-
	6	2.185 - 2.225	81.85	-	-
	7	2.235 - 2.285	74.85	-	-
	8	2.295 - 2.365	66.49	-	-
	9	2.360 - 2.430	59.85	-	-
TIR	10	8.125 - 8.475	-	3040.136402	1735.337945
	11	8.475 - 8.825	-	2482.375199	1666.398761
	12	8.925 - 9.275	-	1935.060183	1585.420044
	13	10.25 - 10.95	-	866.468575	1350.069147
	14	10.95 - 11.65	-	641.326517	1271.221673

It is important to note that the described approach calculates reflectances and brightness temperatures at TOA. The same measures at surface level could be estimated using a radiative transfer code that accounts for atmospheric effects. However, the applied cloud masking algorithm is based on TOA measures and it is assumed that cloud field characteristics are insensitive to the choice of surface or TOA radiance.

### 3.1.3. ASTER sample image

It was already mentioned that ASTER is well suited for an investigation of small cumulus clouds. Figure 2 shows a sample image to demonstrate the characteristics of a typical ASTER scene. Reflectance values are calculated from band 3 (nadir) according to Equation 3.2. The gray-scale image is similar to what one can see with the human eye, bright clouds above the dark ocean surface. It shows precisely the location and structure of individual clouds. The upper part of the image is dominated by clusters of larger clouds while in the lower part there are fewer clouds and occurring more scattered. Clouds of all sizes up to about 10km can be seen. In Chapter 5 the spatial pattern and the cloud size distribution in ASTER images is investigated in more detail.

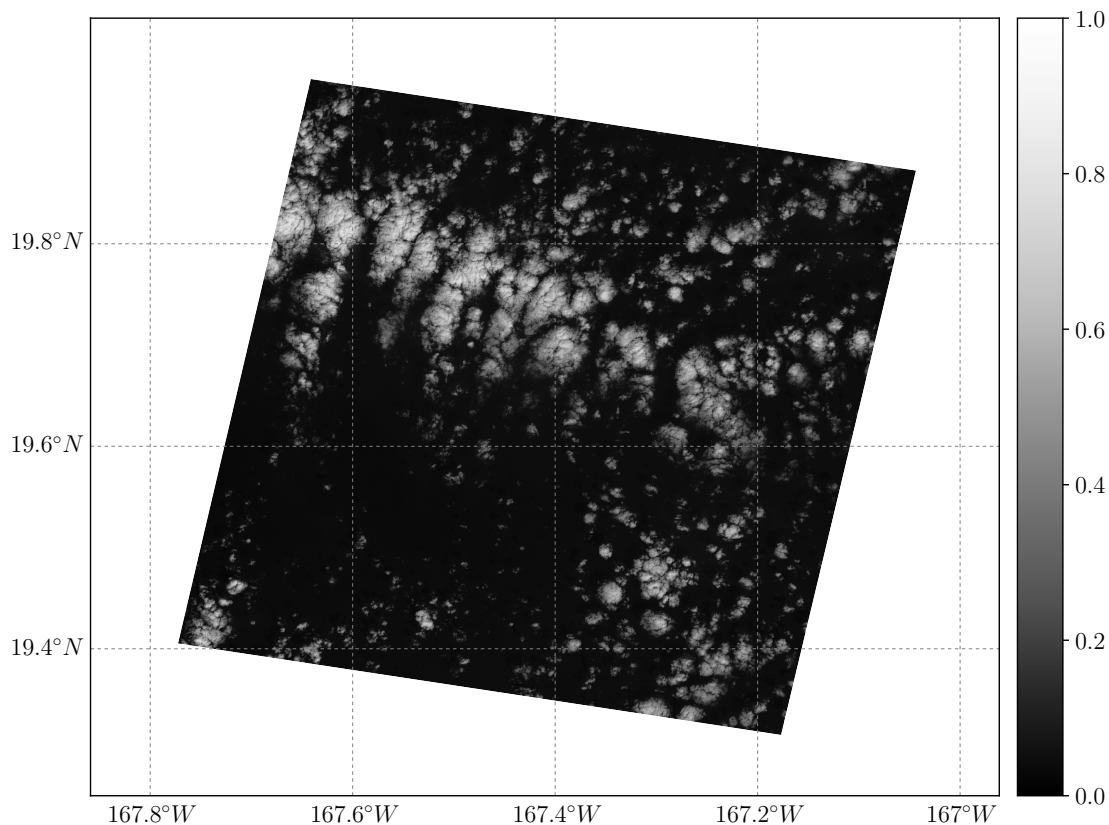


**Figure 2:** Gray-scale ASTER image of reflectance values observed in the visible band 3 (nadir,  $0.76\text{--}0.86\ \mu\text{m}$ ) on the 20<sup>th</sup> of January 2003 at 21:56:19 UTC near Hawaii in the Pacific ocean. The granule covers an area of  $60 \times 60\ \text{km}^2$ .

### 3.2. MODIS cloud products

The ASTER dataset is supplemented with satellite data from MODIS. MODIS is operated by the National Aeronautics and Space Administration (NASA) and also flies on Terra. 36 spectral bands provide information from  $0.414\ \mu\text{m}$  to  $14.235\ \mu\text{m}$  at spatial resolutions of 250 m, 500 m or 1000 m [King et al., 2003]. The imager saves data granules every 5 minutes. Within this time period it covers an area of about 2000 km along-track and 2330 km across-track with the swath edge corresponding to a view angle of about  $55^\circ$ . The current version of MODIS products is Data Collection 6, available at  $1 \times 1\ \text{km}^2$  or  $5 \times 5\ \text{km}^2$  resolution depending on the cloud-top parameter. The pixel spatial resolution decreases towards the swath edge due to the increasing view angle. However, such artefacts as well as limb cooling correction can be safely neglected in this study because the ASTER swath is right in the middle of the MODIS swath, leading to a near-nadir view geometry.

Variables from different data products are relevant for the current study. The MOD06\_L2 dataset includes the Cirrus Reflectance Flag at 1 km resolution. Pixels can be classified as non-cirrus, cirrus or even contrail pixels. This information

is later used to ensure that cirrus clouds do not contaminate the ASTER dataset. The corresponding latitude and longitude information comes from the MOD03 georeference product. MOD06\_L2 also includes a cloud mask at 1 km resolution. This cloud mask is not explicitly needed for the current study on ASTER images, but merely has the purpose of a later comparison and qualitative validation of the derived ASTER cloud mask. In addition, MOD05\_L2 includes water vapor measurements from thermal infrared bands at 5 km resolution. MODIS has five bands around the  $0.94\ \mu\text{m}$  water vapor absorbing band specifically chosen for water vapor retrievals. The thermal infrared retrieval is favored here over the near-infrared retrieval product because the latter does not retrieve values for thin and broken clouds [King et al., 2003].

All MODIS products are spatially and temporally collocated with the ASTER images. First, the closest 5-minute MODIS granule is selected for an ASTER image. Second, MODIS products are resampled to the 15 m ASTER resolution. Depending on the application such a high resolution is not always needed. For example, for water vapor only a scene-average value is considered, therefore averaging over MODIS low resolution pixels within the ASTER scene is sufficient (see Chapter 6.1).

### 3.3. ERA-Interim reanalysis data

ERA-Interim is a global atmospheric reanalysis dataset from the European Centre for Medium-Range Weather Forecasts (ECMWF). It combines forecast and observational data in a consistent format going back to 1979 and being extended continuously up to the present. Detailed information on the ERA-Interim dataset can be found in Dee et al. [2011] and Berrisford et al. [2011].

While surface parameters are available every three hours, upper atmospheric parameters are only available at 00, 06, 12 and 18 UTC. For consistency, surface and profile variables are obtained on a six-hour basis and are downloaded for the time period 2000 to 2007 covering the temporal range of all selected ASTER scenes described in Chapter 4.1. The data is available at a horizontal resolution of  $0.25^\circ$  on a reduced Gaussian grid ( $\sim 30\ \text{km}$ ). In the vertical, variables are available on 37 pressure levels. Depending on the variable and the application certain levels are extracted for the current study. Height levels start at 1000 hPa, decrease in 25 hPa steps until 750 hPa and continue in 50 hPa steps in higher parts of the atmosphere.

From the surface dataset the sea surface temperature (SST), the total column water vapor (TCWV) and the  $u$ ,  $v$  wind components are used. For each ASTER image the ERA-interim analysis field closest in time is selected, either the 12 UTC, 18 UTC or the 00 UTC of the following day. Concerning the spatial collocation, the same re-gridding procedure as described for MODIS is applied. For each ASTER scene, average values are calculated for SST, TCWV, and the wind speed, the latter being the vector sum of the two wind components.

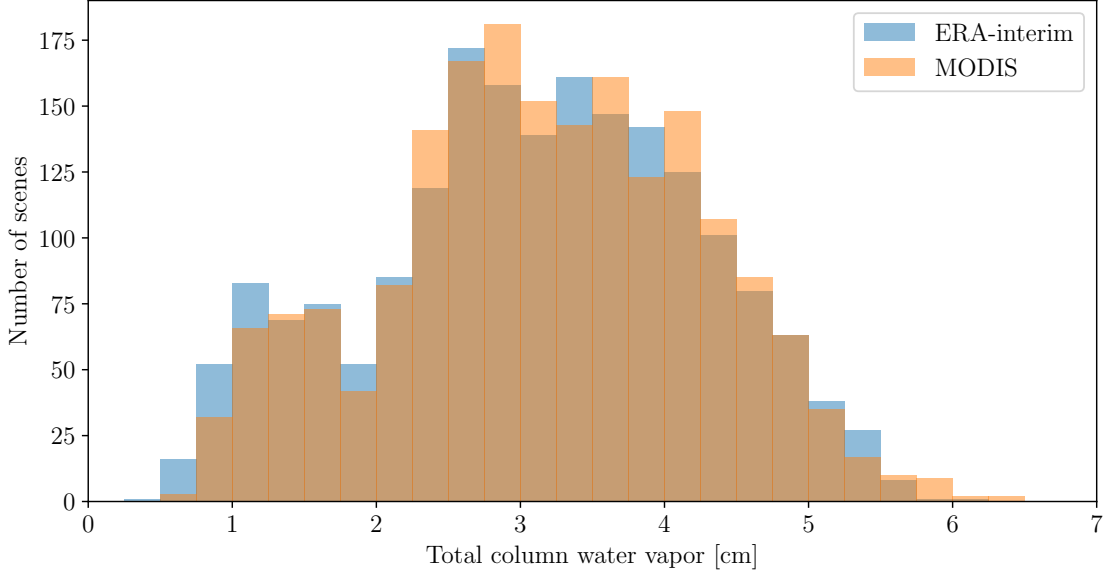


**Figure 3:** Distribution of scene-average total column water vapor from MODIS and ERA-interim reanalysis corresponding to the 1917 ASTER images. The bin width is 0.25 cm.

The model derived scene average TCWV values agree well with the ones calculated from MODIS observations. Figure 3 show the frequency distributions of both datasets, which follow a bimodal distribution. MODIS TCWV is considered to be more accurate due to more precise temporal agreement with ASTER images. Therefore, in the current work, the focus is put on the MODIS dataset. Analysis results for the ERA-interim TCWV can be found in the appendix.

In addition to the surface variables, temperature and wind components are downloaded at 1000 hPa and 700 hPa respectively. The temperature is used to estimate the Lower Tropospheric Stability (LTS) defined as the difference in potential temperature at those two atmospheric levels.

$$LTS = \overline{\Theta}_{700} - \overline{\Theta}_{1000} \quad (3.4)$$

with

$$\overline{\Theta}_{1000} = \overline{T}_{1000} \cdot \left( \frac{P_{1013.25}}{P_{1000}} \right)^{R/c_p} \quad (3.5)$$

and similarly for  $P_{700}$ .  $P$  refers to the pressure,  $T$  to the temperature,  $c_p$  is the specific heat capacity and  $R$  is the gas constant of air.

The wind components are used to calculate the bulk wind shear, that is, the change in wind speed and wind direction from 1000 hPa up to 700 hPa. The vertical velocity

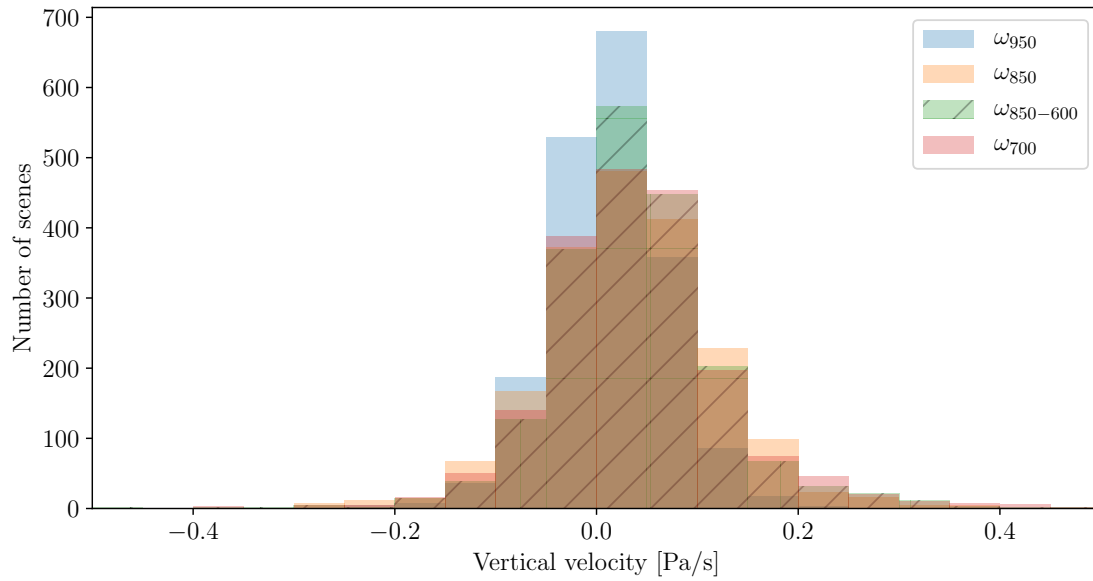


**Figure 4:** Distribution of scene average vertical velocity values from ERA-interim reanalysis at 700 hPa, 850 hPa, 950 hPa and an average of all layers between 850 hPa and 600 hPa for the 1917 ASTER images. Negative values correspond to rising motion, while positive values depict subsiding motion.

is thought to be one of the constraining parameters of the trade wind layer and therefore is taken into account in the current study. Frequency distributions of vertical velocity at various pressure levels are shown in Figure 4.

## 4. Methodology

The present study aims to investigate the macrophysical and organizational characteristics of shallow cumulus clouds in the typical trade wind regions. In this section, the study area is described and several constraints are defined for conditionally selecting suitable images from the ASTER archive. In the second part, a method for deriving a high resolution cloud mask is introduced followed by its validation.

### 4.1. ASTER scene selection

The study area is located in the Northern Hemisphere covering the Atlantic and the Pacific westwards of the US coast up to and including the Hawaiian Islands. Regions over and close to landmasses are excluded. From a first filtering no cumulus cloud fields in ASTER scenes in the East Atlantic are found and, thus, the domain coordinates are reduced to  $180^\circ\text{W} - 40^\circ\text{W}$  and  $0^\circ\text{N} - 50^\circ\text{N}$  (see Figure 5). This is a slight extension of the typical trade wind region and includes deep convective regions around the equator and regions along the Pacific US coast where strato-cumulus clouds dominate [Sandu et al., 2010]. The idea is to filter out shallow cumulus clouds from objective constraints based on the specified cloud type instead of a specific region. Furthermore, the domain covers very different meteorological conditions. If there are shallow cumulus clouds throughout the domain it is interesting to find out constraining meteorological parameters to those clouds.

A limitation of the ASTER archive is the scarce availability of cloudy scenes over the ocean due to the mission's main goal of creating a clear-sky dataset of land surfaces. In addition, scenes are only stored when requested for specific scientific projects. From the ASTER archive images are available along the northern and middle American coastlines. An exceptionally large amount of images is available north-east of Barbados Island in the Atlantic ocean (see Figure 5). Those were recorded during the RICO experiment in 2004 [Zhao and Di Girolamo, 2007]. Concerning the time period covered, ASTER images are available from the beginning of 2000 until present. Starting in May 2007 the SWIR detector suffered temperature problems, which are obvious from image striping and saturation effects. Thus, images are only considered before mid 2007.

Despite the mentioned restrictions on data availability there are still several thousand ASTER images between 2000 and 2007 showing deep convective clouds, as well as stratocumulus and broken trade wind cumulus clouds. The following criteria are applied to select scenes containing trade wind cumulus cloud fields.

- Only daytime images are considered. During daytime the short wave bands can be used in the cloud detection algorithm.

- Images with instrument failure are removed. Two types have been detected, either there are data gaps in images or images show obvious striping especially in the thermal bands.
- Concerning the cloudiness, an upper and a lower limit is defined: An image is considered when there are clouds present and only up to about 80 % cloudiness. The upper limit aims to include cloud fields in transition from stratocumulus to broken cumulus, but to exclude overcast images. This is also a technical aspect since the presence of individual cloud objects is essential in the later statistical analysis of cloud size distributions.
- Images with cirrus clouds are excluded. This turned out to be a major constraint since many images showing shallow cumulus clouds are contaminated by high-level cirrus. Thin cirrus clouds are almost transparent in the visible bands, but can easily be detected in the thermal ASTER bands due to their relatively cold cloud top temperature.

From visually inspecting the ASTER images it becomes obvious that the appearance of clouds strongly depends on the gain settings of the instrument. Cloud detection algorithms should be based on the radiance at the sensor where gain settings are included or further parameters but not on pure digital numbers (see Chapter 3.1.2).

After a first preselection of ASTER images according to the above defined conditions about 2350 scenes remained. In a second visual check the reflectance in band 3 (nadir), the brightness temperature from band 14, the cloud mask described in Chapter 4.2, and the Cirrus Reflectance Flag from MODIS are displayed side-by-side for each ASTER image. Images are excluded when the cloud mask poorly represents the clouds in the visible and thermal bands or cirrus clouds are present. The remaining 1917 ASTER scene locations are shown in Figure 5. Figure 6 shows their temporal distribution throughout the year. During boreal summer, when the ITCZ moves north, few shallow cumulus cloud fields are detected in the study domain. Deep convective clouds are known to dominate during that time period. In boreal winter large-scale subsidence dominates, which is generally connected to typical trade wind cumulus patterns [Nuijens et al., 2014].

## 4.2. ASTER cloud mask

In the literature numerous methods are described to detect clouds in satellite images. Each cloud detection algorithm is designed to serve a specific purpose. The ASTER science team developed the cloud masking algorithm ASTER Cloud Coverage Assessment Algorithm (ACCAA) in 1996 with the aim of detecting cloudy images that cannot be used for land emission studies or in constructing digital elevation models. The algorithm lacks basic spectral tests to detect cirrus clouds and cloud shadows [Hulley and Hook, 2008]. Thus, it does not suit the purpose of the

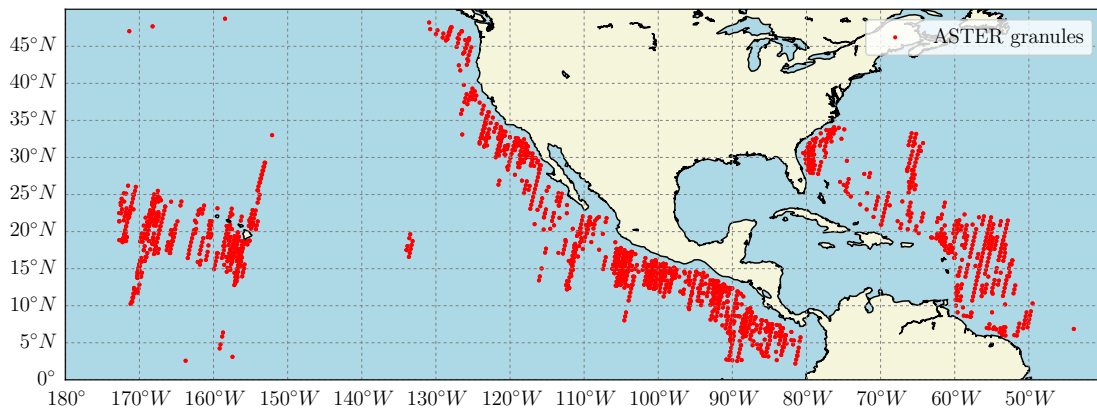


**Figure 5:** The geographical distribution of the ASTER dataset collected between 2000 and 2007. 1917 images are depicted by red squares and show typical shallow cumulus clouds.

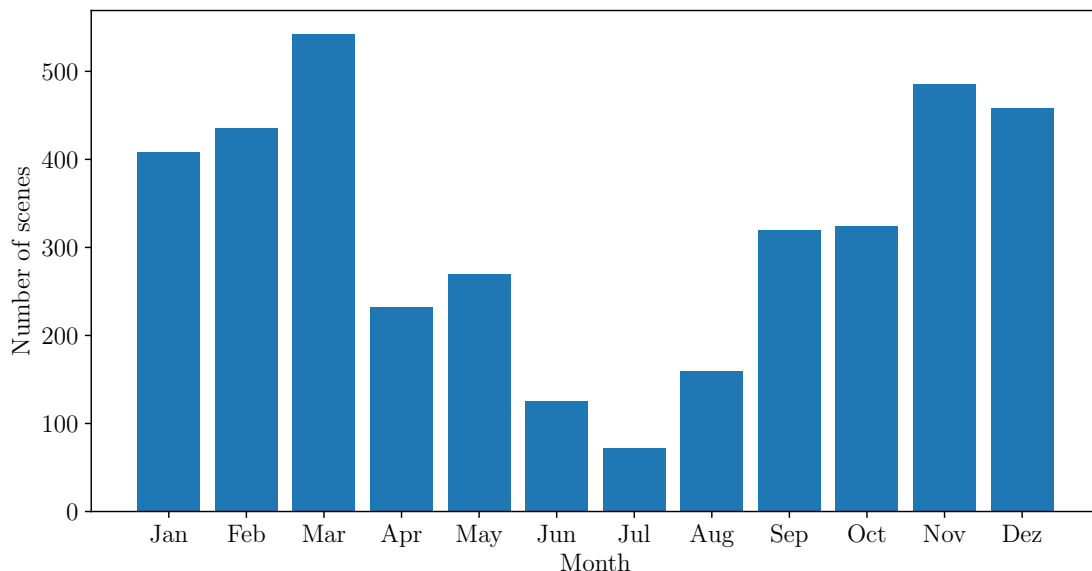


**Figure 6:** Seasonal distribution of the 1917 ASTER images collected between 2000 and 2007.

current study. Other high-resolution cloud studies are based on visually derived cloud masks or use either a single threshold approach in a visible or a thermal band [Cahalan and Joseph, 1989] or a combination of two thresholds [Benner et al., 1998]. Zhao and Di Girolamo [2007] for example, distinguish between clear and cloudy pixels based on a manually tuned threshold for ASTER’s band 3 (nadir) at  $0.76\text{--}0.86\ \mu\text{m}$  (digital number of the original L1B data). In this manual approach the threshold needs to be determined separately for each scene, making it very difficult to analyze a large number of images.

**Table 3:** ASTER clear-cloudy pixel separation based on reflectances  $r$  in the VNIR and SWIR bands 1, 2, 3 (nadir), and 5. The four tests are part of the cloud masking algorithm introduced by Werner et al. [2016].

Flag	Test 1	Test 2	Test 3	Test 4
<i>cloudy</i>	$r_{3N} > 0.065$	$r_5 > 0.02$	$0.80 < r_{3N,2} > 1.75$	$r_{1,2} < 1.2$
<i>probably cloudy</i>	$r_{3N} > 0.03$	$r_5 > 0.015$	$0.75 < r_{3N,2} > 1.75$	$r_{1,2} < 1.35$
<i>probably clear</i>	$r_{3N} > 0.03$	$r_5 > 0.01$	$0.70 < r_{3N,2} > 1.75$	$r_{1,2} < 1.45$
<i>clear</i>	other	other	other	other

Lonitz [2014] developed a more systematic reflectance threshold for ASTER band 3 images assuming that reflectances mainly vary in time with the solar zenith angle. For each month of the year she derived a threshold two times the average minimum reflectance which is assumed to be the reflectance of the ocean. This method was tested but proved to be very sensitive to sun glint and cirrus clouds (see Appendix A.1). Thin cirrus clouds that are almost transparent in the visible can be seen as a cold layer in the thermal frequency range. A cloud detection algorithm similar to the operational ones from MODIS or Landsat is pursued, combining the information from visible and thermal bands.

Just recently, Werner et al. [2016] introduced an algorithm specifically designed for cloud detection in ASTER images. Five thresholding tests similar to the MODIS cloud detection lead to a cloudiness mask on a 15 m resolution, where each pixel can be classified as *clear*, *probably clear*, *probably cloudy*, and *cloudy* (following Platnick et al. [2003]).

The first two tests are designed to distinguish highly reflectant clouds from the dark ocean using the reflectances from ASTER band 3 (nadir),  $r_{3N}$ , and band 5,  $r_5$ , at  $0.86 \mu\text{m}$  and  $2.1 \mu\text{m}$  respectively. 30 m pixels from band 5 are resampled to the VNIR 15 m resolution for a direct pixel-to-pixel comparison. Test 3 additionally accounts for clouds over land surfaces. It uses the ratio of reflectances from band 3 and band 2 ( $0.65 \mu\text{m}$ ),  $r_{3N,2} = r_{3N}/r_2$ . These three tests are usually sufficient to detect bright cumulus clouds. Test 4 is specifically designed to detect cloud edges and very thin cumulus clouds. Again, a ratio of reflectances in the near-infrared range is used  $r_{1,2} = r_1/r_2$  (band 1,  $0.52 \mu\text{m}$ ).

The thresholds in Table 3 were derived by Werner et al. [2016] from 210 ASTER images obtained between April 2003 and July 2007 over the Atlantic and Pacific ocean. The four tests are based on reflectances only and tend to fail in cases with sun glint or under complex broken cloud conditions. Therefore, an additional test based on the brightness temperature from band 14 ( $11.65 \mu\text{m}$ ) is used to correct warm ocean pixels that are labeled cloudy from test 1 to 4. The threshold is set to the 5<sup>th</sup> percentile of brightness temperature values,  $T_B$ , from strictly *clear* pixels in an image, that is, if  $T_B > T_{B,p5}$  the flag is changed to *clear*. The threshold al-

lows slight variations in the temperature of the ocean. Werner et al. [2016] set the condition that the test only applies if more than 3% of *clear* pixels are available in an image. However, applying the algorithm showed that in cases with strong sun glint the 3% condition cannot be met. When adding the *probably clear* flagged pixels at this point, cloud masks can be retrieved. Therefore, the original condition is changed to include *probably clear* pixels with a manual and visual plausibility check of the resulting cloud mask. A complete decision tree describing the cloud masking algorithm can be found in Figure 3 in Werner et al. [2016].

Figure 7 shows an ASTER image recorded on the 15<sup>th</sup> of September 2004 over the Atlantic ocean at different steps of the ASTER cloud mask processing. In Figure 7a reflectances from band 3 ( $0.86\ \mu\text{m}$ , nadir) exemplify the information content from the visible bands used in tests 1 to 4. It is plotted in grey-scale and similar to what one can see with the human eye in this specific case of only shallow clouds over a homogeneous dark ocean surface. High reflectances from cloud tops are white, whereas low reflectance values correspond to dark and absorbing ocean.

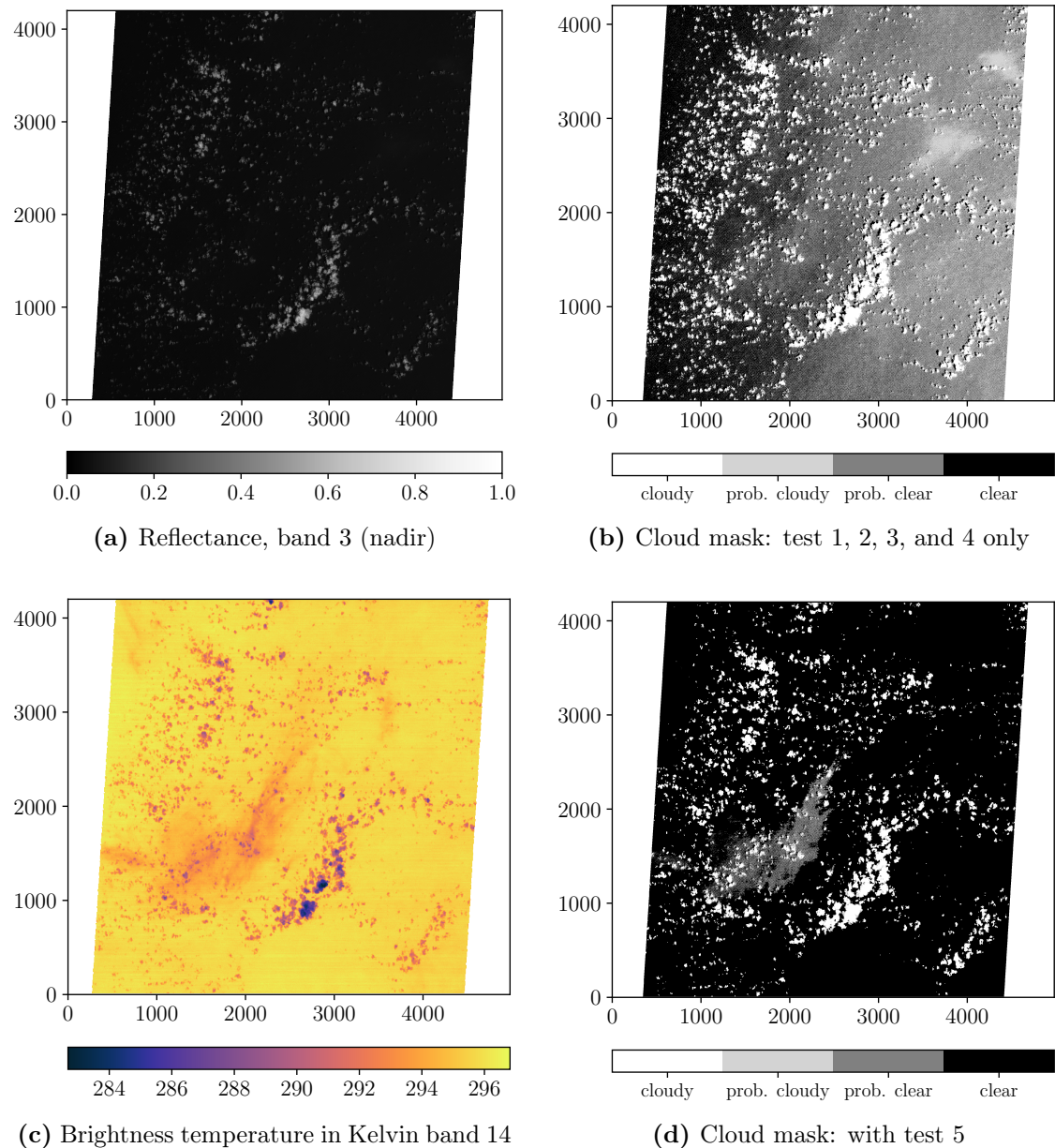
Test 1 based on band 3 reflectances together with test 2, 3, and 4 result in the cloud mask depicted in Figure 7b. At first sight, white areas in Figure 7a are flagged *confidently cloudy* and dark ocean pixels tend to be flagged clear. However, towards the right edge of the image obvious ocean pixels are increasingly flagged *probably clear* or *probably cloudy*. The sun-satellite geometry at the specific time, as well as the visually apparent brighter right side of the image, suggest sun glint to be the major cause. Information from a thermal band can help in detecting sun glint cases.

Figure 7c shows a false-color image of brightness temperatures from ASTER's thermal band 14 ( $11.65\ \mu\text{m}$ ). Two things are obvious: First, the area of pronounced uncertain pixels in Figure 7b corresponds to warm ocean pixels in Figure 7c confirming the sun glint hypothesis. Second, in the mid to lower left corner a relatively cold area shows up that is invisible in the VNIR bands. This cold area most probably corresponds to a high and almost transparent cirrus cloud.

In the final cloud mask in Figure 7d the uncertain pixels due to sun glint are changed to *confidently clear*, while pixels contaminated by cirrus retain their flag of either *probably clear* or *probably cloudy*.

### 4.3. Validation of the ASTER cloud mask

Werner et al. [2016] validate their objective ASTER cloud mask algorithm against the manually constructed cloud masks from Zhao and Di Girolamo [2007] for 152 ASTER scenes over the tropical western Atlantic collected during the RICO campaign. They find a good agreement in the cloud fraction. The cloud mask from Zhao and Di Girolamo [2007] only distinguishes between clear and cloudy pixels.



**Figure 7:** ASTER images recorded on the 15<sup>th</sup> of September 2004 at 14:05:57 UTC at different steps in the cloud masking algorithm. (a) shows reflectances from the VNIR band 3 ( $0.86\ \mu\text{m}$ , nadir) in grey-scale, (b) is the corresponding cloud mask with four cloudiness classes after applying test 1 to 4, (c) is a false-color image of brightness temperatures from ASTER’s thermal band 14 ( $11.65\ \mu\text{m}$ ), and (d) is the final cloud mask including test 5, which uses information from (c).

For a direct comparison, the four classes from Werner et al. [2016] need to be merged to provide a binary classification of clear or cloudy. From a cloud conservative point of view one could only take *cloudy* pixels to represent clouds. However, randomly selected sample images showed a better agreement in cloudiness derived

from the two cloud masks if *cloudy* and *probably cloudy* flagged pixels are combined for the cloud mask constructed according to Werner et al. [2016]. Figure 8 shows the resulting cloud masks for the test case on the 15<sup>th</sup> of September 2004 that is also used in the previous chapter.

For a quantitative comparison of the automated cloud masking algorithm of Werner et al. [2016] against the manual reference from Zhao and Di Girolamo [2007], the cloud fraction, the cloud size distribution, and the fractal dimension are calculated from the two cloud masks and are compared to results from Zhao and Di Girolamo [2007]. The derivation is described in detail in Chapter 5. Some of the ASTER images used by Zhao and Di Girolamo [2007] show obvious cirrus clouds and are excluded. From the remaining dataset of 105 scenes the cloud fraction, as well as the cloud size distribution and fractal dimension agree well. Corresponding figures can be found in Appendix A.1.

Based on the above, it is decided that the automated cloud mask adequately serves the purpose of this study in detecting shallow cumulus clouds in the trade wind region.

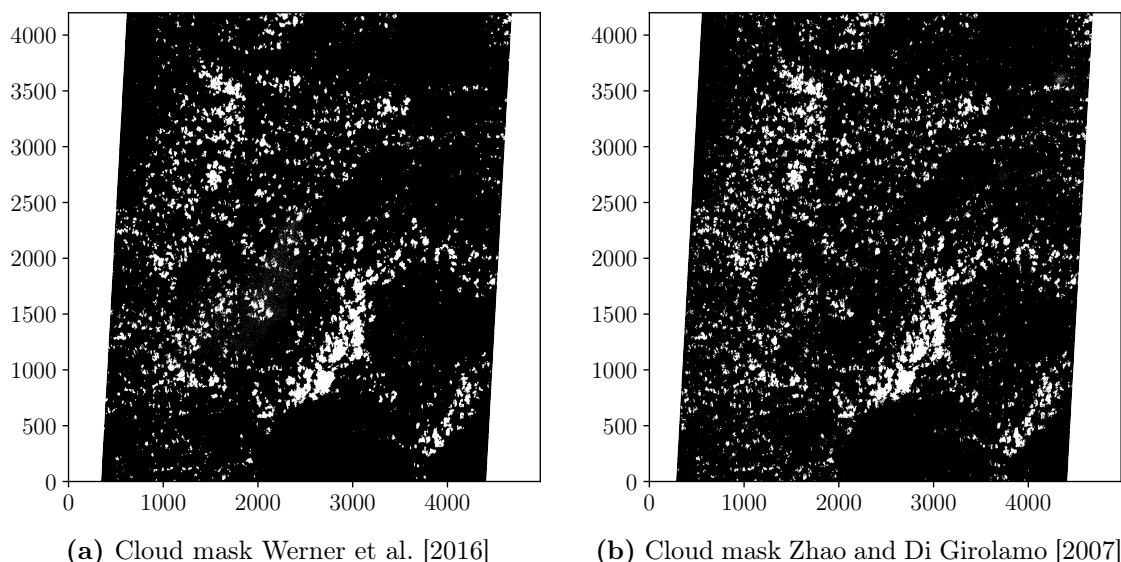


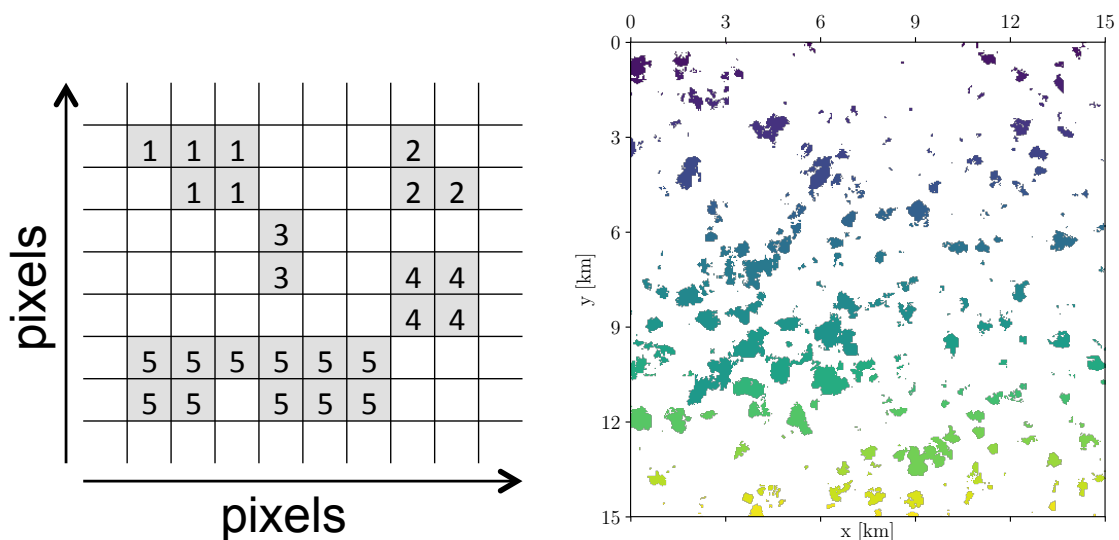
**Figure 8:** ASTER cloud mask for an image recorded on the 15<sup>th</sup> of September 2004 at 14:05:57 UTC. In (a) the algorithm from Werner et al. [2016] is used, while (b) is based on a manually set threshold for band 3 (nadir) digital numbers listed in Zhao and Di Girolamo [2007]. Black pixels correspond to the dark ocean surface and white pixels represent clouds.

#### 4.4. Cloud labeling method

The ASTER cloud mask provides the basis for the statistical analysis of cumulus cloud fields in the following chapters. For this purpose, connected cloudy pixels are defined as individual cloud entities. Two common ways exist for the grouping of connected pixels, 4-connectivity or 8-connectivity. The 4-connectivity rule means that cloudy pixels belong to the same cloud entity if they share a common edge. Cloudy pixels sharing only a vertex, but not an edge belong to separate clouds. 8-connectivity, on the other hand, would include pixels with common vertexes, too. Neither definition of a cloud is inherently superior to the other, but 8-connectivity is less frequently applied in the literature. Figure 9a visualizes cloud labeling using 4-connectivity, which is applied in the current study.

The computation is done with the use of the image processing software package scikit-image for python. Details can be found in the Scikit manual provided by the Scikit image development team [2017]. Pixels belonging to the same cloud entity are labeled with the same integer value.

Analyzing all 1917 ASTER cloud masks showed an anomalously high number of single-pixel clouds. Instrument noise might be the reason for such artificial clouds, which are excluded from any further analysis. More than eight million shallow cumulus clouds larger than one pixel in size are detected in the images. The macrophysical properties of these clouds are analyzed in detail in the following chapter.



(a) Sketch showing the 4-connected cloud labeling approach. Separate clouds are labeled with consecutive integers.

(b) Zoom into a sample ASTER cloud mask showing 4-connected clouds in different colors for a  $15 \times 15 \text{ km}^2$  domain.

**Figure 9:** Cloud labeling approach using the 4-connectivity rule. (a) shows a sketch of the image processing and (b) is part of a sample ASTER image showing identified clouds.

## 5. Cloud field properties from ASTER images

Observational knowledge on the macrophysical properties of shallow cumuli help to understand and model cumulus cloud formation and development in the trades. The irregular shapes of individual clouds complicates their representation in general circulation models. Cloud field properties, such as the cloud fraction and the cloud size distribution, are used in cloud parametrization schemes to account for radiative and latent heating effects. The cloud size distribution is especially important. It is used to calculate the mass flux and energy transported within individual clouds depending on the cloud area and the cloud vertical velocity [Neggers et al., 2003]. Modeled cloud fields are often validated by comparing cloud size distributions to those found in observations. The high resolution ASTER dataset is particularly well suited to investigate the properties of small trade wind cumuli.

This chapter introduces physical and statistical measures to describe cloud fields captured in the ASTER images, which were obtained between 2000 and 2007 over the Pacific and Atlantic ocean. The cloud fraction, cloud size distribution as well as spatial distribution are discussed, followed by a chapter on physical parameters assumed to control such cloud field properties.

### 5.1. Cloud fraction

The cloud fraction is a simple measure quantifying the part of the sky that is obscured by clouds. For each ASTER image the cloud fraction is calculated by dividing the number of cloudy flagged pixels by the total number of pixels. Swath edge pixels are neglected as well as single cloudy pixels or 1-pixel clouds, which are assumed to result from instrument noise (see Chapter 4.4).

The cloud fraction calculated of individual ASTER images ranges from 0–40 % with an average of 11.78 %. The frequency distribution of cloud fraction is shown in Figure 10. About 90 % of the images have a cloud fraction of less than 25 %. The mean cloudiness is in broad agreement with findings from Zhao and Di Girolamo [2007], where 152 ASTER images were analyzed during the RICO campaign in 2004 with an average cloud fraction of 8.6 %. Brueck et al. [2015] find a higher cloud fraction from two years of cloud observations at the BCO with an average of about 30 %. However, clouds considered in the study by Brueck et al. [2015] are not limited to shallow cumulus clouds, but include all cloud types in the lower troposphere.

### 5.2. Cloud top height

Shallow cumulus clouds mostly have cloud top heights within the trade wind boundary layer. The boundary layer height typically varies between 1–2 km [Stevens, 2005], but cumuli reaching up to 3–4 km are also observed [Nuijens and Stevens,

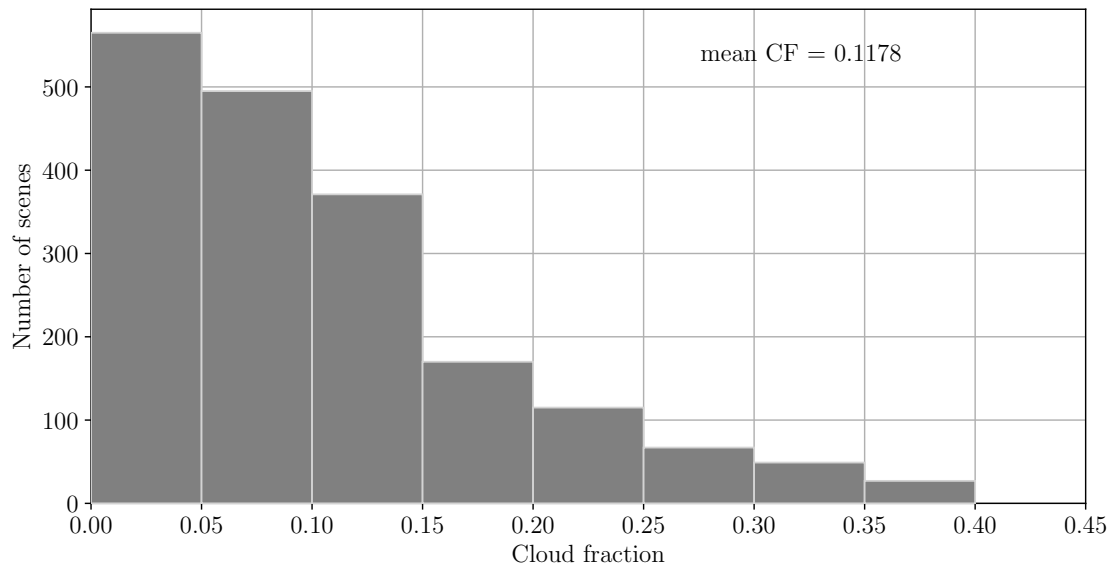


**Figure 10:** Frequency distribution of cloud fraction in 1917 ASTER images. The cloud fraction is calculated as the ratio of cloudy to the total number of 15 m pixels in the ASTER cloud mask.

2012]. Furthermore, studies focusing on precipitating shallow cumulus clouds suggest that the onset of precipitation is coupled to the cloud depth. Assuming a rather constant cloud base height at about 700 m leaves precipitation depending only on the cloud top height. In Lonitz [2014] the threshold cloud top height is set to 3 km and it is shown that precipitating trade wind cumuli organize differently compared to non-precipitating ones. Thus, the question arises whether shallow clouds sampled in the ASTER dataset have cloud top heights above 3 km.

The cloud top height (CTH) can be derived by matching the measured cloud top brightness temperature to a temperature profile, either from a nearby sounding or from reanalysis data. However, collocated radiosonde profiles are scarcely available for the temporally and spatially scattered ASTER scenes. Model profiles often miss low-level temperature inversions, leading to an overestimation of low cloud heights by more than 2 km. To overcome these shortcomings, Baum et al. [2012] propose a variation of the infrared-window approach for estimating the cloud top height in the MODIS Collection 6 cloud top product. Cloud height is calculated from the difference in the brightness temperatures of cloudy and clear pixels observed at  $11 \mu\text{m}$  divided by the apparent lapse rate  $\Gamma$  in  $[K/km]$ , which is derived with the help of Calipso lidar cloud-top height measurements. The  $11 \mu\text{m}$  band is best suited for the retrieval because the water vapor absorption is low.

When calculating the brightness temperature of cloudy pixels in ASTER TIR images (see Chapter 3.1.2) a cloud emissivity of  $\epsilon = 1$  is assumed. This assumption is more likely valid for fully cloudy TIR pixels. To minimize a low bias in cloud top

heights, a value is only retrieved for a 90 m TIR pixel if all included 15 m visible-channel pixels are flagged cloudy in the corresponding cloud mask (see Chapter 4.2). Similarly, a TIR pixel is considered clear if all 15 m visible-channel pixels within it are flagged clear. For each ASTER image an average surface brightness temperature  $BT_{clear}$  is calculated from these fully clear 90 m pixels. Equation 5.1 is used to calculate cloud top heights from brightness temperature values of cloudy pixels  $BT_{cloudy}$ :

$$CTH = \frac{BT_{clear} - BT_{cloudy}}{\Gamma} \quad (5.1)$$

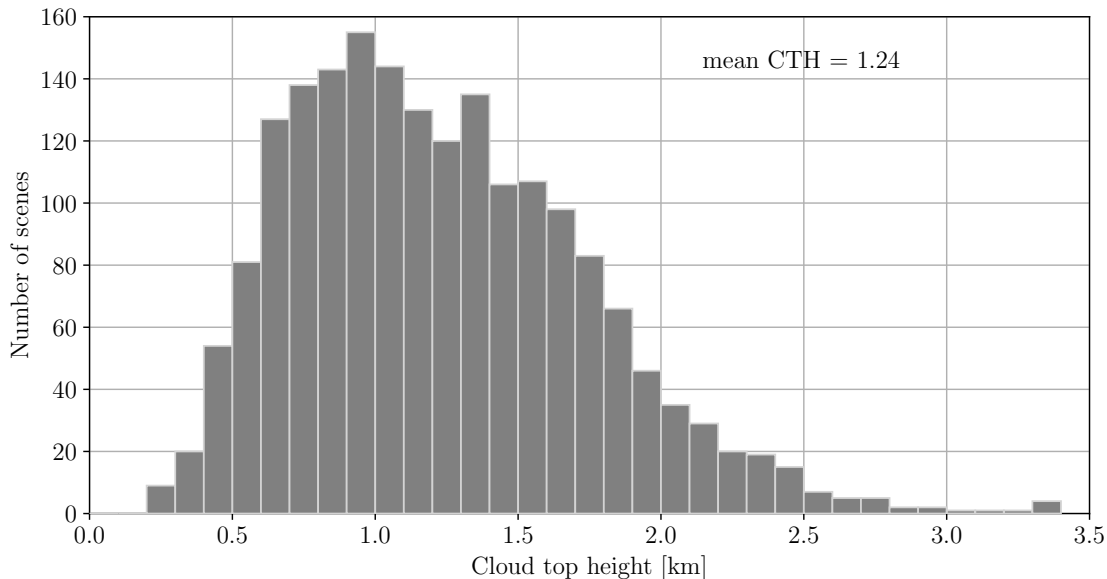
where  $\Gamma$  is the apparent lapse rate in [ $K/km$ ]. Values for  $\Gamma$  can be derived from a lookup table published in Baum et al. [2012]. The authors provide a season- and latitude-dependent lapse rate that is approximated by a 4<sup>th</sup> order polynomial. Thus, only date and geolocation information is needed to calculate the corresponding  $\Gamma$  for each ASTER image.

Figure 11 shows the distribution of scene-average CTHs in the ASTER dataset. A clear peak occurs at about 1 km while the distribution decays towards higher cloud tops. In the cloud top height study of Genkova et al. [2007], trade wind cumuli exhibit a bimodal frequency distribution with maxima at 650 m and 1500 m. from 157 ASTER scenes collected during the RICO campaign in 2004. Although the CTH distribution in Figure 11 shows a minor second maximum at 1.5 km, it is not significant enough to be claimed to be a second peak. In addition, the frequency distribution of CTHs of single pixels shows an even smoother decay in the distribution towards higher cloud tops than ASTER scene-average CTHs (see Appendix A.2).

It is important to keep in mind that several factors add uncertainty to the CTH retrieval. First of all, a high bias from water vapor above the clouds might occur. Zhao and Di Girolamo [2007] estimate such a water vapor induced uncertainty to up to 200 m. On the other hand, Genkova et al. [2007] show that ASTER cloud top heights calculated by a stereoscopic retrieval result in more accurate and lower height estimates. They show that the ASTER infrared-window retrieval has a low height bias of about 250 m on average compared to the stereo height retrieval. These opposing effects can partially cancel out. The CTHs in the current study are assumed to have an uncertainty of 200 – 300 m.

### 5.3. Cloud shape

Cloud models often assume circular cloud shapes together with a cloud size distribution in their parametrization schemes. The analyzed ASTER images show clouds with sizes ranging over several orders of magnitude. The question arises whether all sizes are equally represented or whether one cloud size is dominant.



**Figure 11:** Frequency distribution of scene-average cloud top heights from 1917 ASTER images. The cloud top height is only derived for fully cloudy TIR pixels with a 90 m resolution and then averaged for each ASTER image.

And do they have circular shapes or rather ragged shapes? In the following, the appearance of cumulus clouds detected in the ASTER images is investigated. The cloud size distribution is discussed along with a measure related to the perimeter.

### 5.3.1. Cloud size distribution

The size of a cloud is calculated from the sum of all pixels belonging to the same cloud entity multiplied by the pixel area defined by the cloud mask resolution (15 m x 15 m). The distribution of cumulus cloud sizes was subject to several studies in the past stating different functional relations for the cloud size density, that is the number of clouds  $n(D)$  of a given size  $D$ . Wielicki and Welch [1986] find an exponential cloud size distribution, while López [1977] suggests a lognormal distribution. Most popular and most frequently used is a power law behavior (Cahalan and Joseph [1989], Benner et al. [1998], Zhao and Di Girolamo [2007]). Some studies claim a single, others a double power law with a scale break to best represent the cloud size density. Zhao and Di Girolamo [2007] give a comprehensive review of former cloud size distribution analysis from high-resolution imagery and the obtained parameters describing the distribution. The general form of the power law is defined by:

$$n(D) = aD^b \quad (5.2)$$

where  $n(D)$  is the cloud size density,  $D$  is the cloud size and  $b$  is the slope parameter. The slope parameter gives information about which cloud sizes contribute most

to the total cloud fraction. A steep slope for example means that small clouds are dominating. The total number of clouds can be calculated by integrating Equation 5.2 over all cloud sizes  $D$ :

$$n = \int_0^{\infty} n(D)dD \quad (5.3)$$

According to Neggers et al. [2003], the cloud size distribution is often plotted on a double logarithmic scale. In Figure 12 the normalized cloud size distribution of all clouds detected in the ASTER dataset is plotted. Again, 1-pixel clouds are excluded. The cloud equivalent diameter (eqd) is a measure of the cloud size. It is calculated from the cloud area assuming a perfectly circular cloud. Note that the size distribution changes with the chosen bin width. However, a more detailed study of the effect of the bin width is beyond the scope of this work. Following a discussion in Zhao and Di Girolamo [2007] the bin width is set to 100 m.

Assuming a power law according to Equation 5.2 the distribution is described by the power law exponent  $\lambda$ . When plotting the size distribution on a double logarithmic scale, the power exponent can be derived from a linear fit to the distribution. Neggers et al. [2003] describe the relation of the cloud size density on a logarithmic to that on a linear scale by the following equation:

$$\begin{aligned} n(\log(D)) \cdot d(\log(D)) &= n(D) \cdot dD \\ n(\log(D)) &= n(D) \cdot \frac{dD}{d(\log(D))} \\ &= n(D) \cdot D \cdot \ln(10) \end{aligned} \quad (5.4)$$

Substituting Equation 5.2 gives:

$$\begin{aligned} n(\log(D)) &= aD^b \cdot D \cdot \ln(10) \\ &= (a \cdot \ln(10)) \cdot D^{b+1} \\ &= \text{const} \cdot D^{-\lambda} \end{aligned} \quad (5.5)$$

In Figure 12 such a linear fit to the size distribution is represented by the blue line with the slope  $\lambda_{single} = 2.85$ . A linear fit puts equal weights on all sizes. However, larger clouds are less frequently sampled, potentially leading to a bias. To avoid this an upper limit of 10 km are used for the fitting and the derivation of the slope  $\lambda$ . The value of  $\lambda_{single}$  is in accordance with the one found by Zhao and Di Girolamo [2007]. Lonitz [2014] proposes a power exponent  $b = 1.21$  and accordingly  $\lambda_{single} = 2.21$  from one year of ASTER images in the Caribbean. Note that some studies report values for  $b$  while others refer to  $\lambda$ , which are related according to Equation 5.5 by  $\lambda = b + 1$ .

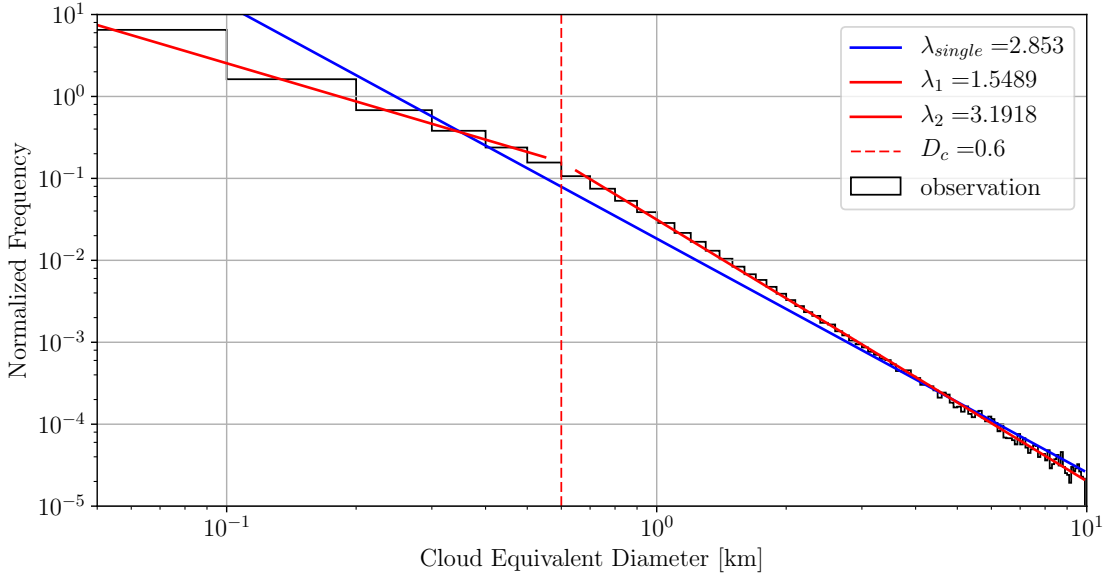


**Figure 12:** Frequency distribution of cloud equivalent diameters of all clouds detected in 1917 ASTER images (1-pixel clouds are excluded). The black steps represent the distribution on a double logarithmic scale with a 100 m bin width. The blue line shows the fit of a single power law to the bin centers of the distribution with the power exponent  $\lambda_{single}$ , while the red solid lines show the double power law fit with slopes  $\lambda_1$  at small sizes and  $\lambda_2$  at larger sizes. The scale break size  $D_c$  (red dashed line) is located where the double power law fits result in a minimum combined least-squared error.

Benner et al. [1998] show that the majority of their studied cumulus cloud field images are best represented by a double power law. Therefore, in a second step, fits are performed separately for small and large clouds represented by two red solid lines in Figure 12. The threshold cloud size, the so called scale break size  $D_c$ , is defined such that the two least-squares fits result in the smallest combined error. Here, a separation at  $D_c = 600$  m in the size distribution is found with the corresponding slopes  $\lambda_1 = 1.55$  (for  $D < D_c$ ) and  $\lambda_2 = 3.19$  (for  $D > D_c$ ).

Table 4 summarizes findings from other observational and modeling studies. For cloud equivalent diameters below the scale break, all studies find a slope  $b > -2$  and for cloud equivalent diameters above the scale break  $b$  stays below  $-2$ . Neggers et al. [2003] only derive one exponent up to a cut off at the scale break size and suggest that no clear behavior can be found for larger cloud sizes.

In general, small clouds are much more numerous than large ones. However, the question is which clouds contribute most to the total cloud cover, that is, whether it is the many small ones or rather the few large ones. Neggers et al. [2003] derive a relation of cloud size and cloud fraction based on the cloud size distribution. According to them, the total cloud fraction is proportional to  $D^{b+2}$  for a single power law meaning that for  $b > -2$  large clouds dominate the cloud fraction and smaller clouds for  $b < -2$  respectively. In other words, the cloud fraction increases with

Study	$\lambda_1$	$b_1$	$\lambda_2$	$b_2$	$D_c[m]$
Cahalan and Joseph [1989]		0.89		2.76	500
Neggers et al. [2003] (*)		0.70		-	400 - 1250
Benner et al. [1998]	1.98		3.06		900
Zhao and Di Girolamo [2007]	1.88		3.18		600
This study	1.55		3.19		600

**Table 4:** Summary of slope parameters and scale break from cloud size distributions from different observational and modelling (\*) studies.  $\lambda$  and  $b$  are related according to Equation 5.5.

the cloud size up to the size of the scale break and decreases again for cloud sizes  $D$  greater than  $D_c$ . The derived  $\lambda_{single}$  of 2.85 indicates that large clouds contribute most to the total cloud fraction compared to small ones in this study. Knowledge on the cloud sizes contributing most to the cloud fraction is important in the validation by observations of cloud fields from Large-eddy simulations (LESs).

Potential mechanisms controlling the scale break are widely discussed. Cahalan and Joseph [1989] relate the scale break to the fact that the largest possible cluster size is limited by the boundary layer depth, while Neggers et al. [2003] suggest a connection between the scale break and cloud-subcloud layer interactions.

On the other hand, there is also criticism of the various existing scale break theories. Heus and Seifert [2013] suggest that poor sampling of large clouds produces a change in the slope of the size distribution.

Peters et al. [2009] find that cluster properties like the size distribution change with column water vapor. The authors hypothesize that former studies find different functional forms of the size distribution because they mix atmospheric states characterized by differing water vapor contents. Based on percolation theory they show that for certain column water vapor values the size distribution exhibits a scale-free behavior without a scale break. However, Peters et al. [2009] analyzed coarse resolved mesoscale convective systems and thus, their findings might not be applicable to small trade wind cumulus clouds.

The slope of the size distribution in Figure 13  $\lambda_{area}$  of 2.01, which is based on the actual cloud area, is remarkably close to that of a two-dimensional critical percolation given by Peters et al. [2009] to be  $187/19 \approx 2.06$ . Figure 13 is similar to Figure 12, but the cloud size is characterized by the area instead of the equivalent diameter. The bin width and range are adjusted accordingly. An adequate bin width of  $0.07 \text{ km}^2$  was derived from applying the Scott's rule introduced in Scott [2010]. The bin width  $w$  depends on the standard deviation  $\sigma$  and the number of samples  $n$ :  $w = 3.49 \cdot \sigma \cdot n^{-1/3}$ .

A cloud area of  $0.07 \text{ km}^2$  is equivalent to a cloud equivalent diameter of about 300 m. The range of cloud areas up to about  $80 \text{ km}^2$  corresponds to the previously defined 10 km cloud equivalent diameter.

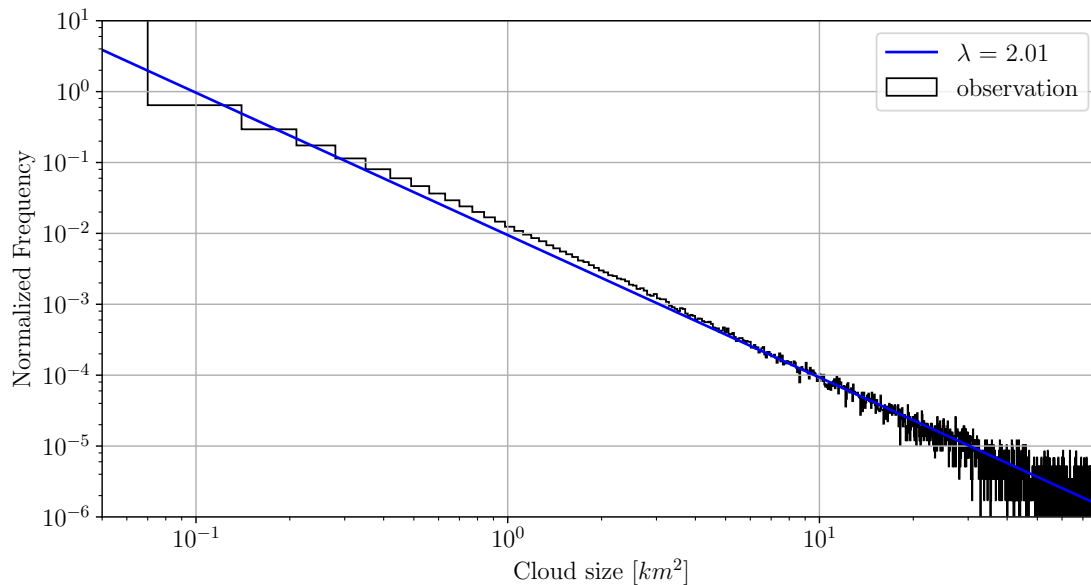


**Figure 13:** Frequency distribution of cloud areas observed in 1917 ASTER scenes (single-pixel clouds are excluded). The black steps represent the distribution on a double logarithmic scale with a  $0.07 \text{ km}^2$  bin width. The blue line shows the fit of a single power law to the bin centers of the distribution with the power exponent  $\lambda$ .

The result of the observed distribution slope with that from percolation theory would imply that the observed cloud fields are rich in scales. On the other hand, if simple percolation were the dominating factor, little could be learned from statistical parameters describing cloud fields, because such parameters are mainly the result of geometric effects rather than any physical processes.

A scale-free behavior would be in contrast to many studies arguing for the existence of a scale break size. Stevens [2005] even suggests the scale break to be a controlling parameter of the size distribution of shallow cumulus clouds. Another aspect supporting the scale break theory is given by the natural scale of eddies in the boundary layer of about 500 m. The vertical extent is directly linked to the horizontal one meaning that one would expect clouds to exhibit a typical size of about 500 m, which is close to the scale break size found in Figure 12.

Parameters controlling the cloud size distribution are still a matter of ongoing research. This topic is further evaluated in Chapter 6. In the following, additional parameters are introduced to characterize single clouds as well as cloud fields.

### 5.3.2. Fractal dimension

Lovejoy [1982] applied Mandelbrot's theory of fractals to cloud shapes. He argues that clouds can be seen as fractals because they have "shapes with structure at all scales, with no characteristic length [...]" meaning that in a statistical sense, they are self-similar. Thus, according to Mandelbrot the relationship between cloud area

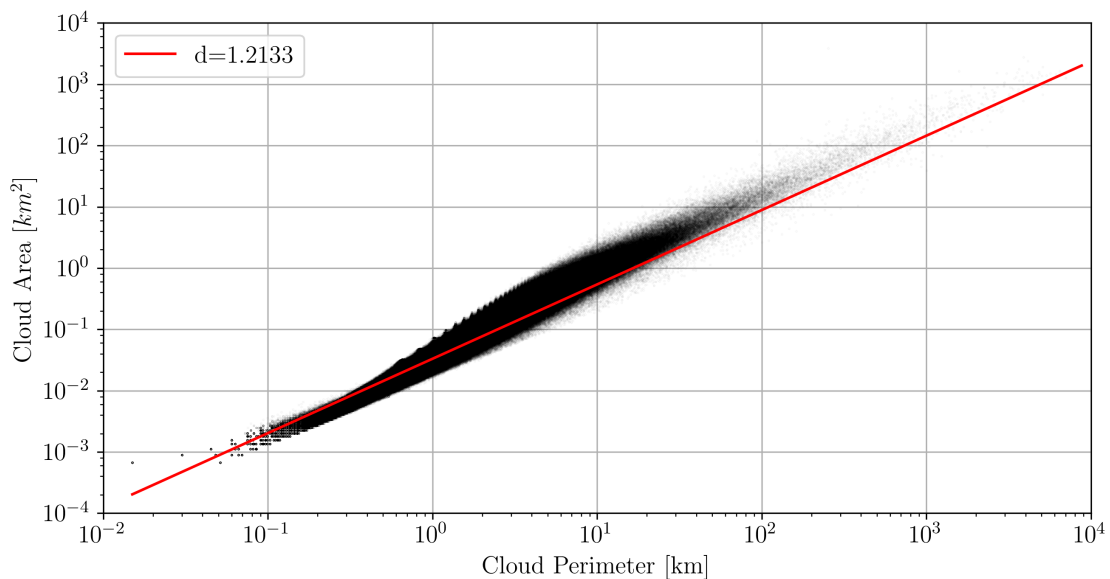


**Figure 14:** Scatter plot of cloud perimeter versus cloud area for all clouds detected in 1917 ASTER images (excluding 1-pixel clouds). The red line is a linear fit on the double logarithmic scale. According to Equation 5.6, the slope estimates the fractal dimension  $d$ .

and perimeter can be used to investigate the complexity of cloud shapes:

$$P \propto (\sqrt{A})^d \quad (5.6)$$

where  $P$  is the cloud perimeter,  $A$  the cloud area and  $d$  the fractal dimension. The fractal dimension of a perfectly circular cloud would be unity while Equation 5.6 transforms to  $P \propto A$  for clouds with increasingly ragged shapes and  $d \rightarrow 2$  respectively. The cloud perimeter can be defined in several ways. Its lower limit is determined by the pixel size. Its upper limit is usually set by the domain size, but is of minor importance in this study since the investigated trade wind cumuli are much smaller than the ASTER domain size. Pixels at the cloud edges are assumed to be partly cloudy. Therefore, the cloud perimeter is calculated by connecting the cloud edge pixel centers and following this border line around the cloud. This procedure results in smoother cloud boundaries compared to walking along the sides of the outermost cloudy pixels of a cloud entity.

In Figure 14 cloud areas are plotted against the corresponding perimeters on a log-log scale for all clouds detected in the ASTER dataset. The fractal dimension  $d$  is derived from a linear least-squares fit. The existence of only one obvious value for  $d$  indicates that there is no characteristic length scale for cloud perimeters. The calculated value of  $d = 1.21$  implies that sampled clouds are rather compact and with smoother shapes compared to former studies, which report higher  $d$ -values (see Table 5).

Study	$d_1$	$d_2$	$D_c$
Cahalan and Joseph [1989]	1.34	1.47	500
Peters et al. [2009]	$\approx \frac{4}{3}$		
Benner et al. [1998]	1.23	1.37	900
Zhao and Di Girolamo [2007]	1.28		
Lovejoy [1982]	1.35		
This study	1.21		

**Table 5:** Summary of fractal dimensions reported in various observational studies. Fractal dimensions are calculated according to Equation 5.6 either assuming a double power law with the fractal dimensions  $d_1$  below and  $d_2$  above the scale break size  $D_c$  or a single power law with the fractal dimension  $d_1$ .

Similar to the cloud area distribution, Peters et al. [2009] find a remarkable agreement of the calculated fractal dimension and the one suggested by gradient percolation theory. The authors distinguish between the accessible hull with a fractal dimension  $d_{acc} = 4/3 = 1.33$  and the full hull with  $d_{full} = 7/4 = 1.75$ . The accessible hull neglects passages in the cloud perimeter that recede into the shape while the full hull resolves the exact outline. Due to the discretization into pixels, a precise derivation of the full hull is impossible. However, in this study the perimeter is calculated such that it is closer to the definition of the accessible hull. A fractal dimension close to that predicted by gradient percolation would suggest that the area-perimeter relation is rather independent of physical processes. As a positive result, cluster boundaries could easily be described in cloud model parametrizations by simple geometric aspects. This would also imply, that the fractal dimension cannot be used in model validation because it tells little about the underlying physics of cloud development. It is also questionable whether a fractal dimension of 1.21 can be considered to be close to the percolation value of 1.33. However, variations in the fractal dimension and its relation to environmental conditions are further investigated in Chapter 6.

It is noted that different ways of constructing the perimeter result in values for  $d$  up to 2 in the current study. Varying definitions of the perimeter might be one reason for different values for the fractal dimension found in the literature.

## 5.4. Spatial distribution

The spatial arrangement of clouds within individual ASTER images can either be classified as random, regular or aggregated. Influencing factors are the domain size and data resolution, as well as the number of clouds and their sizes. In the following, the spatial distribution is analyzed by means of the nearest neighbor distance. An index quantifying the organization of clouds in a cloud field is also introduced.

### 5.4.1. Nearest neighbor analysis

One can get a first impression of the spatial distribution of clouds from calculating nearest neighbor distances. The distance between two clouds is given by the euclidean distance between the pixel coordinates of their geometric centers. This cloud centroid is simply the average position of all cloudy pixels belonging to the same cloud entity. The corresponding mathematical expression for the centroid is:

$$\vec{x}_c = \frac{1}{N} \sum_i^N \vec{x}_i \quad (5.7)$$

with the vector  $\vec{x}_i$  pointing at pixel  $i$  of a given cloud entity. For randomly distributed clouds one would expect a gaussian distribution. A regular distribution has one peak at a favored distance while aggregated cloud fields exhibit a strong peak at the lowest possible distances (limited by the cloud extent) and tail off towards larger distances.

Figure 15 demonstrates that the most frequently found distance of neighboring clouds is about 50 m in the ASTER dataset, with larger distances becoming less frequent. Thus, the shape of the distribution suggests aggregated trade wind cumulus fields. To further investigate the aggregation state the total number of clouds in an ASTER image is also included in the analysis. Tobin et al. [2012] introduce an index, the Simple Convective Aggregation Index (SCAI), to better quantify the degree of aggregation in cloud fields.

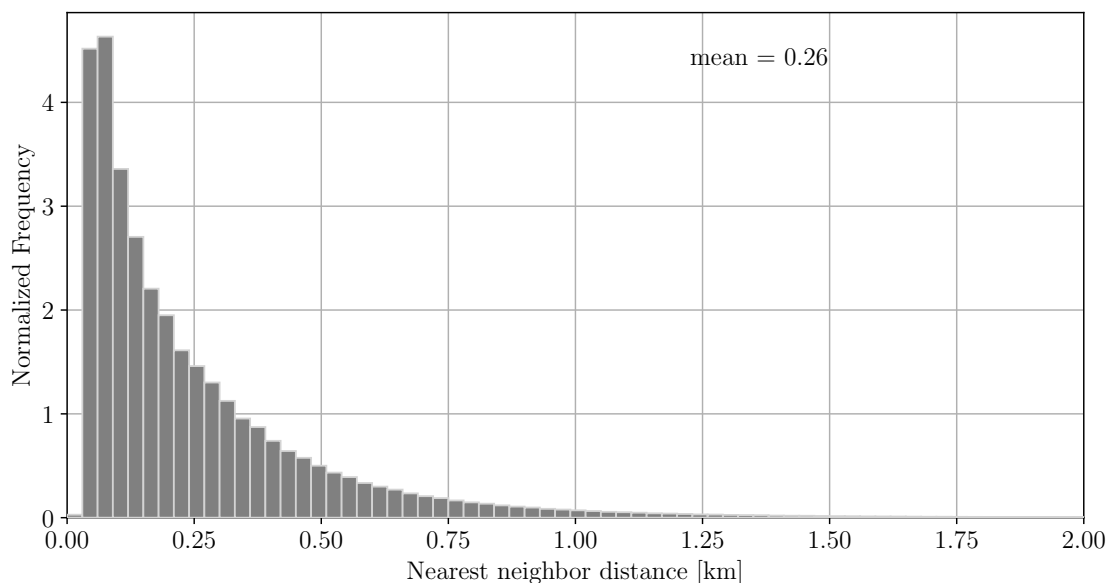


**Figure 15:** Normalized frequency of nearest neighbor distances. The distance is measured between cloud centroids from clouds detected in 1917 ASTER images.

### 5.4.2. Simple Convective Aggregation Index

The simple convective aggregation index (SCAI) is a combination of two features, the number of clouds and the distance in between the clouds. Both are relevant in describing the clustering of points in an ensemble. Fewer clouds are present in more aggregated situations and short distances between the clouds also indicate a higher degree of aggregation [Tobin et al., 2012].

The number of clouds  $N$  is normalized by the maximum possible number  $N_{max}$  within a given domain size, while the measure for the distance between the clouds  $l$  is normalized by the characteristic length scale of the domain  $L$  [Tobin et al., 2012]. That way the aggregation state is normalized by the potential maximal disaggregation.  $N_{max}$  is limited by the domain size, the pixel resolution, and the cloud labeling scheme. In this study with the applied 4-connectivity rule,  $N_{max}$  is half the ASTER granule pixels (excluding swath edge pixels).  $l$  is the geometric mean of all distances  $l_i$  between cloud pairs (see Equation 5.9).  $L$  is set to the length of the diagonal of the 60 km x 60 km ASTER domain. The SCAI index is then calculated for each ASTER scene according to the following equation:

$$SCAI = \frac{N}{N_{max}} \frac{l}{L} \cdot 1000 \quad (5.8)$$

with the distance  $l$ :

$$l = \sqrt[n]{\prod_{i=1}^n l_i} \quad (5.9)$$

One consequence of this definition is that SCAI can increase with  $N$  and independently also with  $l$ . However, these parameters are connected due to the fixed domain size. Thus, a higher number of clouds in an ASTER image would alone lead to a higher SCAI, but SCAI can stay at the same level or even decrease due to a simultaneously decreasing distance between the clouds. However, Tobin et al. [2012] show that  $N$  is dominating the SCAI, which is also obvious from comparing the observed frequency distributions of  $N$  and SCAI in Figure 17 and 16 respectively. In general, low SCAI values are related to aggregated cloud fields and high SCAI values to disaggregated situations.

The distribution of SCAI values in Figure 16 shows that most of the images are characterized by low SCAI values. Mean and median of the distribution are both 0.1 and 80 % of the values are below 0.15. The SCAI values here are by two orders of magnitude smaller than those reported by Tobin et al. [2012] from satellite images with a lower resolution. However, the range is reasonable considering that SCAI depends on the domain size and spatial resolution. Moreover, in a recent study by Stein et al. [2017], SCAI values ranging from 0 to 1.5 are derived from CloudSat-CALIPSO composites and are related to aggregated and disaggregated cloud fields respectively.

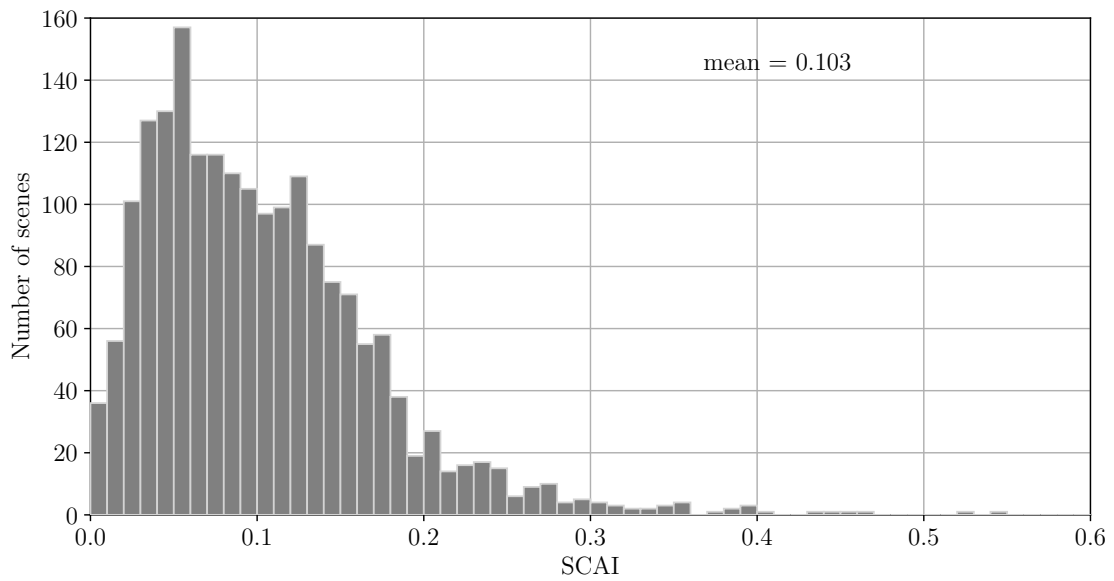


**Figure 16:** Frequency distribution of the simple convective aggregation index (SCAI) calculated for 1917 ASTER images according to Equation 5.8. The bin width is 0.01. The SCAI is a dimensionless parameter introduced by Tobin et al. [2012] that quantifies the degree of aggregation in a cloud field.

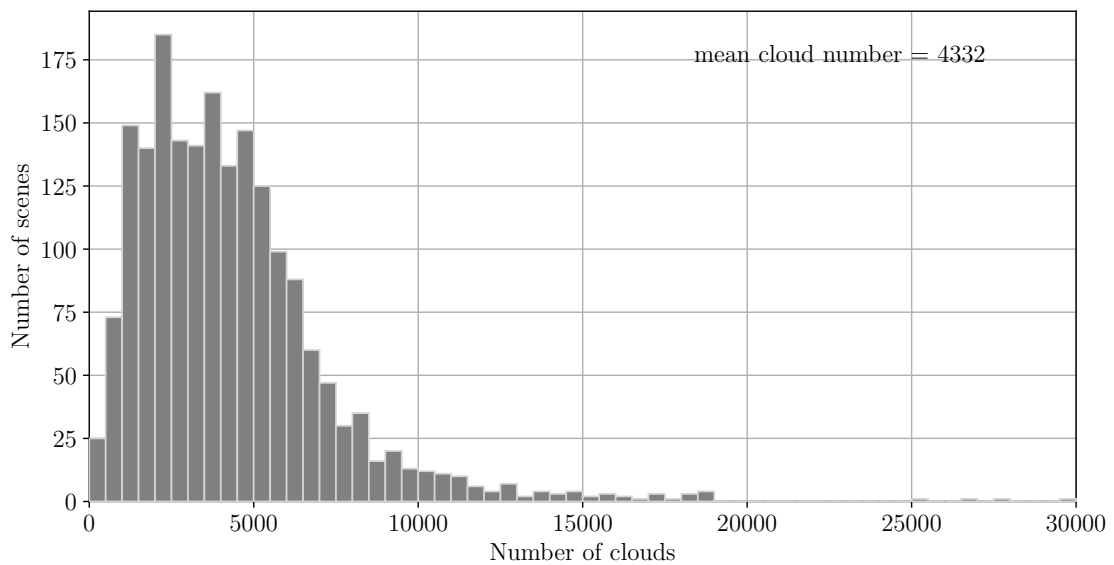


**Figure 17:** Frequency distribution of the number of clouds in 1917 ASTER scenes. The bin width is 500.

## 6. Physical parameters controlling cloud field properties

The mechanisms controlling trade wind cumulus cloud fields are widely discussed in the literature but still considerably uncertain (Nuijens and Stevens [2012], Brueck et al. [2015], Nuijens et al. [2015], Sakradzija and Hohenegger [2017], Bony et al. [2015]). Observations of such small cumulus clouds are scarcely available and existing knowledge is taken from short observational campaigns (RICO: Zhao and Di Girolamo [2007], Nuijens et al. [2009]; NARVAL: Stevens et al. [2017]), localized observations (BCO: Brueck et al. [2015]) or Large-Eddy Simulation (LES) studies of idealized cases (Nuijens and Stevens [2012], Sakradzija and Hohenegger [2017]). From several observational as well as modeling studies, Chris Bretherton suggests the following main controlling factors: the amount of water vapor in the lower troposphere, the depth of the boundary layer and whether shallow cumulus clouds precipitate or not [Chris Bretherton, personal communication, May 2017].

Concerning precipitation, Lonitz [2014] found that shallow cumulus clouds organize differently in precipitating versus non-precipitating cases. Clouds are assumed to precipitate if they exhibit cloud top heights of 3 km and higher. The frequency distribution in Figure 11 shows that the vast majority of the clouds detected in the ASTER dataset do not exceed the 3 km threshold. Therefore, the presence of only non-precipitating trade wind cumuli can be assumed in the current study according to Lonitz [2014]. In the following, the properties of cloud fields are investigated starting with their dependence on moisture in the lower troposphere and the trade wind layer height. The results are discussed in context with other studies.

### 6.1. Moisture in the lower troposphere

Moisture in the lower troposphere determines the potential energy for convective processes. The amount and distribution of moisture within the trade wind layer is of great importance as they relate to the strength of the inversion and radiative cooling. Such processes in turn affect the general circulation [Stevens et al., 2017]. The scale height of water vapor is about 2 km meaning that most of it is concentrated in the lowest 2–3 km of the troposphere. The total column water vapor (TCWV), defined as the mass-weighted integral over the specific humidity, was shown to be linked to thermodynamic and radiative effects of moisture [Stevens et al., 2017].

In the following, the relationship between TCWV and observed cloud field properties is investigated. The distribution of ASTER scene-average TCWV is shown in Figure 18. Two points shall be noted here. First, most cloud fields observed under dry atmospheric conditions ( $< 2$  cm) originate from the North-East Pacific and might be affected by different dynamical conditions compared to the typical

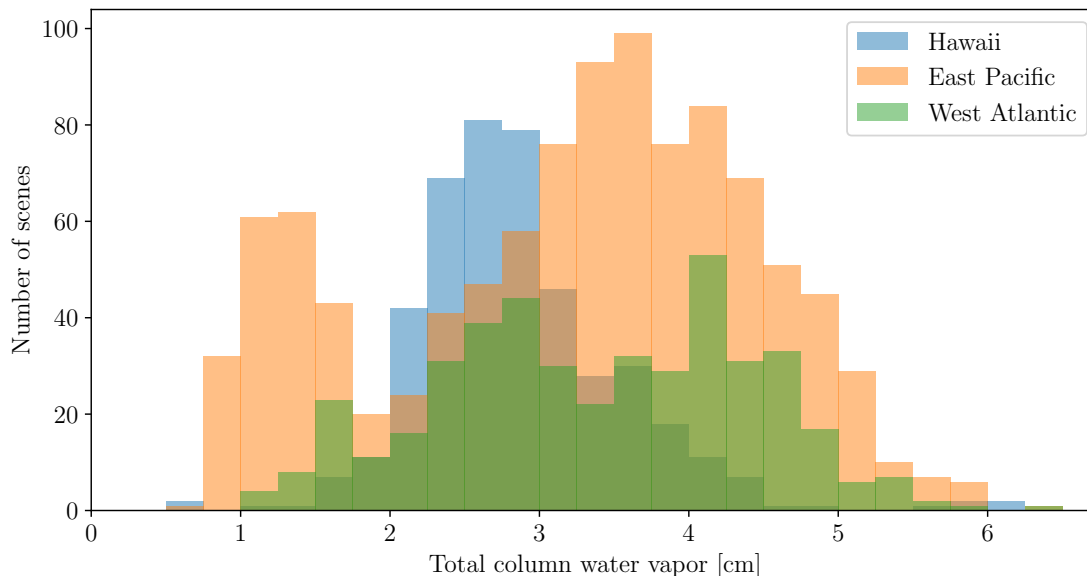


**Figure 18:** Distribution of scene-average total column water vapor (TCWV) from MODIS corresponding to the 1917 ASTER images. The data is displayed separately for three different regions. Scenes located west of  $140^\circ$  W are displayed in blue ('Hawaii'), between  $140^\circ$  W and  $81^\circ$  W in orange ('East Pacific') and east of  $81^\circ$  W in green ('West Atlantic'). The bin width is 0.25 cm.

trade wind regions. Second, the shallow cumulus cloud images cover a large range of moisture values. In the following, the cloud fields are therefore analyzed with regard to their dependence on the amount of moisture. Cloud field properties are calculated separately for subsets of the ASTER dataset corresponding to different TCWV bins to analyze changes with increasing moisture. Five moisture bins are defined for TCWV values of 0–2, 2–3, 3–4, 4–5, and 5–7 centimeters. These bins are chosen such that they include at least 50 values. Choosing strictly equal-sized bins does not change the below results in a qualitative way.

Cloud field properties corresponding to different moisture bins are summarized in Figure 19. The two upper most panels **A** and **B** show parameters that describe the cloud size distribution. Cloud fields in a very moist and a very dry environment seem to exhibit similar cloud size distributions. For intermediate moisture values, the cloud size distribution does not vary significantly. In comparison to the parameters calculated from the whole dataset, denoted with 'total', very dry and very moist situations coincide with less steep slopes of the single power law fits of both, cloud equivalent diameters (panel **A**), as well as cloud areas (panel **B**). A less steep slope indicates larger clouds. Apart from that, the scale break size  $D_c$  represents the double power law fit introduced in Chapter 5.3.1. The large scale break size also suggests the presence of relatively more large clouds and fewer small clouds based on the assumption that the general shape of the distribution does not change.

The dependence of the cloud size distribution on water vapor is extensively discussed in the literature for Mesoscale Convective Systems (MCSs) and deep convection (Peters et al. [2009], Tobin et al. [2012]). Peters et al. [2009] argue, that studies on cloud size distribution that do not distinguish between different water vapor regimes can only find a skewed average of different dependencies of cloud properties. For the cloud radar data investigated in their study a fast decay (small  $\lambda$ ) in the size distribution is found for low water vapor situations and a slow decay for situations with a higher water vapor load. Peters et al. [2009] propose that this behavior can be extrapolated to smaller scales. However, their results for dry conditions are in contrast to findings from the current study. A possible explanation is that very dry situations in the current dataset correspond to ASTER images collected along the North-Western coast of the United States. Cloud fields observed there might be affected by different dynamical processes dominating in the wake of the land masses [Chris Bretherton, personal communication, May, 2017]. In sum, while the interpretation of the driest situations remains unclear, the variation of the cloud size distribution with TCWV for moist situations is unambiguous. More moisture in the lower troposphere provides the potential for larger clouds to form. The fractal dimension displayed in Figure 19 panel **C** is quite independent of moisture changes. Zhao and Di Girolamo [2007] suggest a connection between the fractal dimension and the turbulent flow behavior of clouds. Larger entrainment at the cloud edge might lead to more ragged cloud shapes and accordingly to a larger fractal dimension. Thus, it seems that moisture in the lower troposphere does not change turbulent flows at the cloud edges.

In panel **D**, two values describing the aggregation state are displayed, the simple convective aggregation index (SCAI) and the average number of clouds in an ASTER image. Both parameters slightly decrease from dry towards moist conditions suggesting that cloud fields in a moist environment are more aggregated. However, the dependence is marginal and shows a large uncertainty. The change in cloud fraction in Figure 19 panel **E** shows an unexpected behavior. In general, one would expect higher cloudiness in a moister atmosphere. Here, cloud fraction decreases with increasing moisture, although the change lies within the uncertainty and might not be significant. Brueck et al. [2015] report a similar negative correlation between relative humidity in the cloud layer to low level cloud fraction at the BCO. From two years of cloud observations they find that wet summer months are more frequently associated with low cloud fractions while higher cloud fractions dominate the dry winter months. However, it is emphasized in their study that moisture does not alone control low level cloud fraction. A combination of several factors should be considered including vertical velocity, surface fluxes, and lower tropospheric stability.

It remains unclear how the moisture in the lower troposphere relates to cloud field properties, especially to the aggregation state and cloud fraction. A more detailed study is necessary to further discuss the topic. This is beyond the scope of the current work.

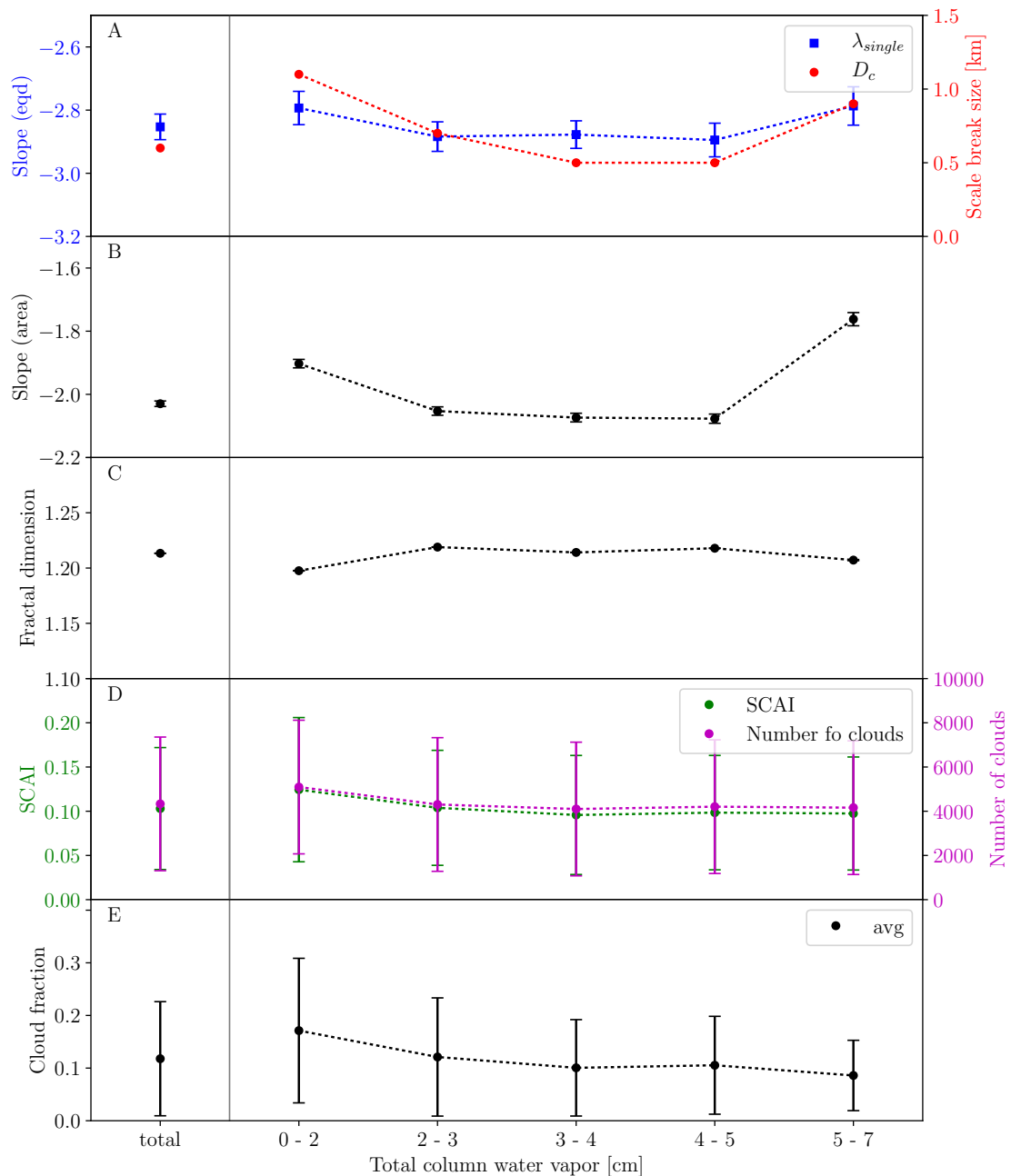


**Figure 19:** Cloud field properties as a function of moisture. ASTER images are sorted into different bins according to the scene-average total column water vapor (TCWV) from MODIS. In **A** the size distribution of cloud equivalent diameters (eqd) is represented by the slope of a single power law fit  $\lambda_{single}$  and the scale break size  $D_c$  of a double power law fit to the distribution. **B** shows the slope of a single power law fit to the actual cloud area. The fractal dimension  $d$  is plotted in **C** while panel **D** indicates the aggregation of the cloud fields by means of the average number of clouds in ASTER images and by the average SCAI. **E** shows the corresponding cloud fraction. The calculation of these parameters is described in detail in Chapter 4. The first column is calculated from the full ASTER dataset denoted 'total' and the other columns correspond to the TCWV that is given at the bottom. Errorbars of average variables, cloud fraction, SCAI, and the number of clouds, represent the standard deviation. Errorbars to variables derived by fitting correspond to the error in the slope, that is the square root of the error covariance matrix.

## 6.2. The trade wind boundary layer height

Factors determining the height of the trade wind boundary layer are manifold. Nuijens and Stevens [2012] propose wind speed to be a major controlling factor for the layer height and the clouds therein using LES simulations. They formulate their hypothesis based on former studies which relate higher wind speeds to an enhanced evaporation over the ocean. This, together with a stronger upward mixing of moisture, increases the humidity in the cloud layer and leads to deeper clouds and a deepening of the trade wind boundary layer. In LES, wind speed alters the surface fluxes, which are defined as the product of wind speed and the difference in temperature or moisture between the surface and cloud base. An increase in wind speed therefore leads to an enhanced moisture and mass flux into the cloud layer jointly leading to a deepening of the trade wind boundary layer.

Concerning the current study, there are two important things to note. First, the deepening of the trade wind layer is associated with higher cloud tops, which can be observed in the ASTER images. Second, the mass flux approach in moist convective parametrization schemes takes the simple product of cloud area and cloud vertical velocity to account for clouds. Therefore, an increase in mass flux is most likely not only related to stronger updrafts but also to larger cloud areas. In addition, a larger vertical extent of the trade wind layer allows for the existence of larger eddies which link the horizontal and vertical scale of clouds, likewise implying the occurrence of larger cloud areas [Brueck et al., 2015]. Therefore, a change in the cloud size distribution, as well as in the cloud fraction is expected.

In conclusion, the working hypothesis for this chapter is that with increasing wind speed the trade wind layer deepens and cumulus clouds have higher cloud tops. The deepening is associated with larger cloud areas, depicted by a less steep slope in the cloud size distribution, and a higher cloud fraction.

To test the hypothesis, the correlation between CTHs and wind speed is analyzed first. The derivation of CTHs from ASTER images is described in detail in Chapter 5.2. The average surface wind speed is taken from ERA-interim reanalysis. The frequency distribution of wind speeds covers a range of up to 15  $\text{m/s}$  (see Figure 20). Lower wind speeds are most frequently observed in the East Pacific. Wind speed bins are chosen to include at least 50 ASTER images to ensure a robust statistical analysis. Regimes are defined in steps of 2.5  $\text{m/s}$  while the last bin includes all wind speed values exceeding 10  $\text{m/s}$ . Figure 21 shows the distributions of CTHs as a function of surface wind speed. An increase of CTH with increasing wind speed above 7.5  $\text{m/s}$  is observed, supporting the findings from LES and bulk concepts in Nuijens et al. [2009].

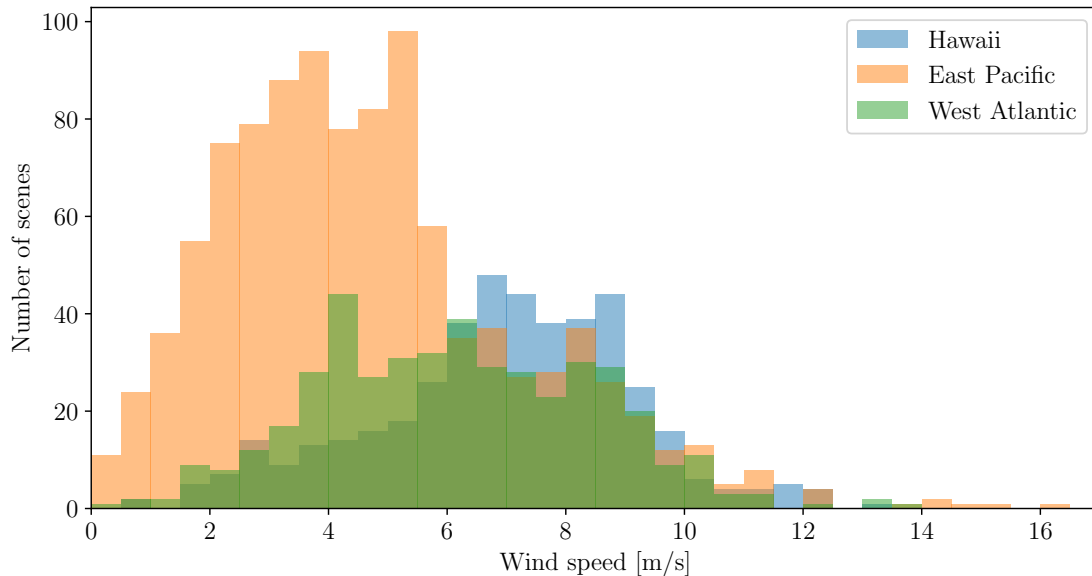


**Figure 20:** Distribution of scene-average wind speeds from ERA-interim data corresponding to 1917 ASTER images. The data is displayed separately for three different regions. Scenes located west of  $140^\circ$  W are displayed in blue ('Hawaii'), between  $140^\circ$  W and  $81^\circ$  W in orange ('East Pacific') and east of  $81^\circ$  W in green ('West Atlantic'). The bin width is  $0.5 \text{ m/s}$ .

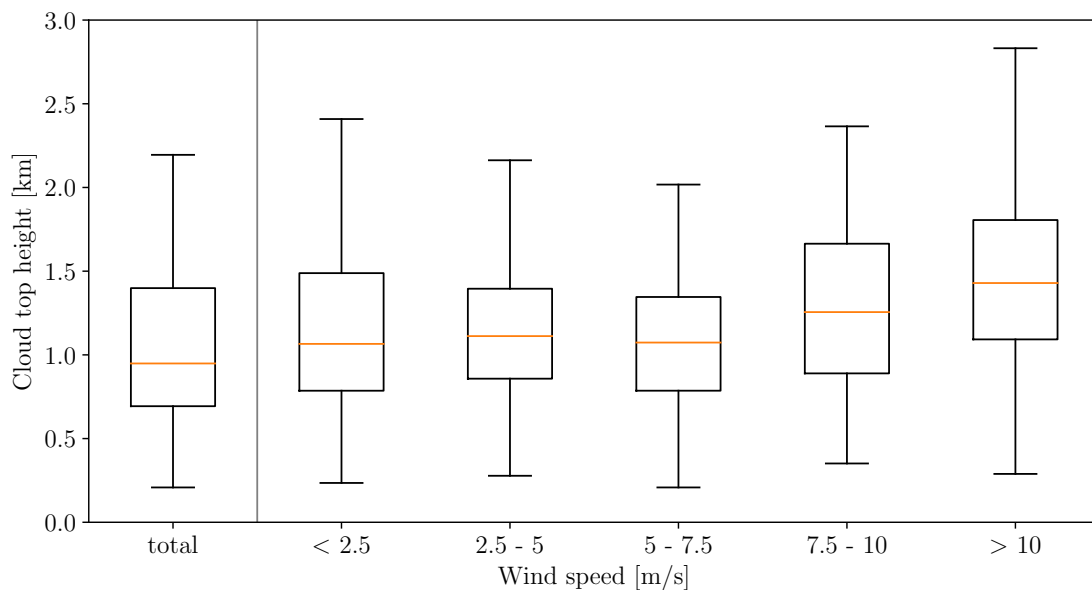


**Figure 21:** Box-whisker plots of scene-average cloud top heights (CTHs) in 1917 ASTER images for different surface wind speeds. The red line denotes the median within each wind speed bin and the black box encompasses values between the  $25^{\text{th}}$ ,  $p_{25}$ , and the  $75^{\text{th}}$  percentile,  $p_{75}$ . The whiskers range from  $[p_{25} - 1.5 \cdot IQR]$  to  $[p_{75} + 1.5 \cdot IQR]$  with the inner-quartile range  $IQR$ .

In the next step, it is investigated whether wind speed also influences other cloud field properties such as the cloud size and cloud spatial distribution. Panel **A** in Figure 22 shows the variation of cloud size distribution with increasing wind speed. The slope of the size distribution assuming a single power law fit,  $\lambda_{single}$ , increases to higher values.  $D_c$  also increases with increasing wind speed from 500 m to 900 m. Both of these results suggest a shift in the size distribution towards larger clouds. Figure 22 panel **B** indicates the same qualitative change in the cloud size distribution but based on cloud area instead of cloud equivalent diameter. Thus, the findings are independent of the definition of the cloud size.

The fractal dimension  $d$  in Figure 22 panel **C** remains constant for wind speeds up to 7.5 m/s and slightly decreases for higher wind speeds, suggesting slightly more compact clouds. The decrease of  $d$  under strong winds seems counterintuitive, since one would expect more ragged cloud shapes (higher  $d$ ). Presumably, the larger clouds associated with strong surface winds have smoother and more circular shapes ( $d \rightarrow 1$ ).

According to Figure 22 panel **D**, wind speed influences not only cloud shapes, but also the spatial distribution of clouds. The increase in SCAI with increasing wind speed suggests that cloud fields are less aggregated. One can easily imagine that strong winds inhibit organized convection, although the exact mechanisms are unclear at this stage. The increase in SCAI is partly due to the increase in the number of clouds in a cloud field (see also Equation 5.8). A larger number of clouds is in disagreement with modeling results from Nuijens and Stevens [2012] who report that the cloud amount does not change with increasing wind speed. However, the underlying LES study has several limitations, such as the low number of simulated cloud fields.

While satellite observations of cloud fields are assumed to capture clouds at different stages in their lifetime, the LES cloud field corresponds to a certain output time when the model is in an equilibrium state. Models react to the deepening of the cloud layer with an increase in downward mixing of dry air from the free troposphere to the surface. Warm and dry air reduces the surface heat flux and surface buoyancy flux. This in turn dampens the initial increase in upward mass flux, which is connected to the deepening of the cloud layer.

In addition, wind shear is neglected in the model although a positive correlation between wind shear and wind speed is shown by Brueck et al. [2015]. Moreover, the large-scale circulation is not accounted for in LES. It seems that controlling parameters of cloud fields cannot be considered separately. Large-scale subsidence, for example, can stabilize the lower troposphere partly suppressing deeper convection and redistributing the energy into smaller clouds. Thus, wind shear, vertical velocity and lower tropospheric stability are additional physical parameters that might control cloud field properties. They are further analyzed in Chapter 6.3.

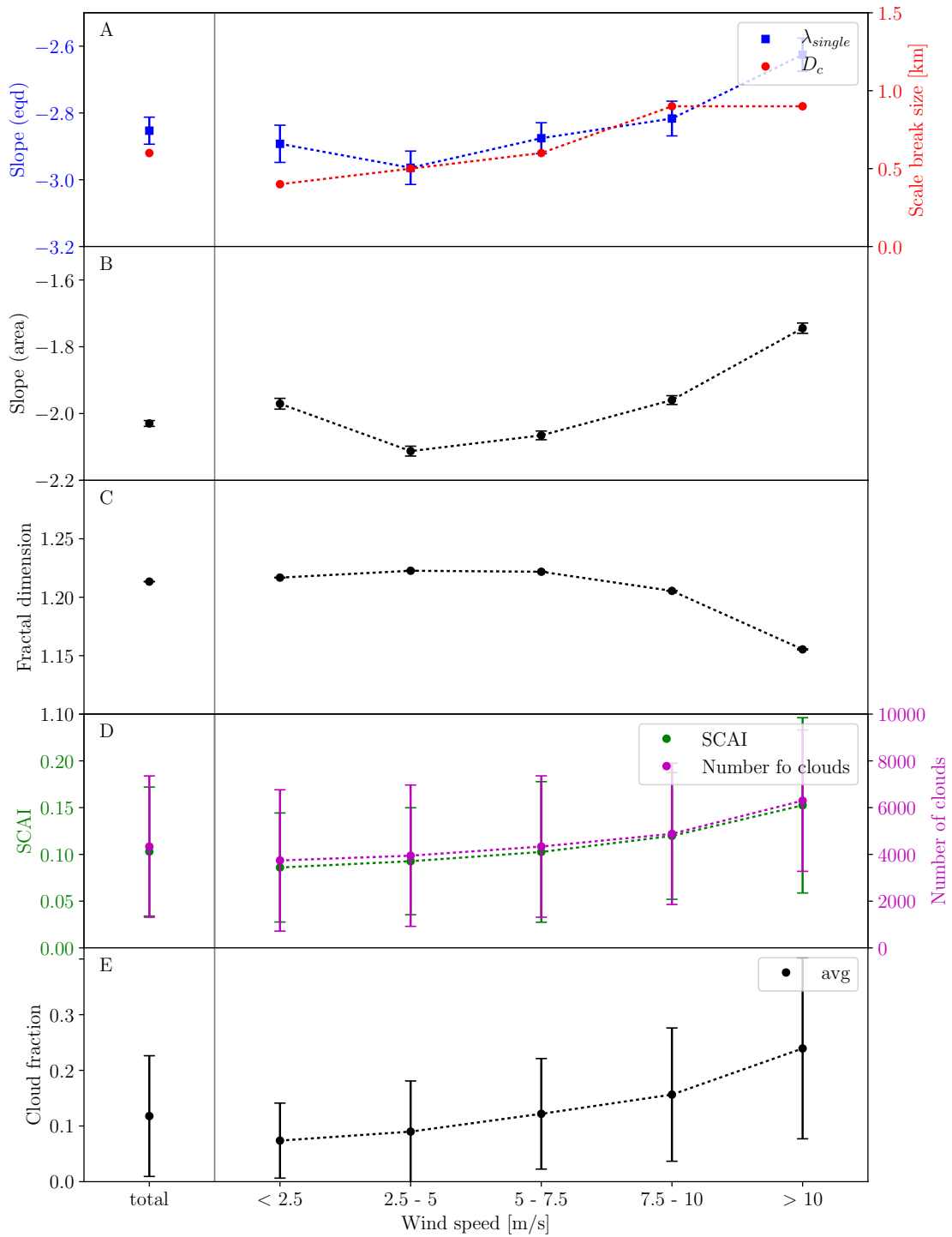


**Figure 22:** Cloud field properties as a function of surface wind speed. 1917 ASTER images are sorted into different bins according to the scene-average wind speed from ERA-interim reanalysis. See the caption of Figure 19 for a full description of the parameters.

In general, the hypothesis is supported by observations: An increase in wind speed deepens the trade wind layer. Clouds are found to be deeper, larger, more compact, and more numerous leading to an increase in cloud fraction as shown in Figure 22 panel **E**. This result is in accordance with the study by Brueck et al. [2015] where wind speed is found to be the major factor controlling low level cloudiness in observational data at the BCO. Dependencies might become even clearer if one can rule out precipitation. Although it is assumed that clouds with cloud top heights less than 3 km do not precipitate [Lonitz, 2014], deeper and larger clouds are more likely to precipitate in general. The onset of precipitation would counteract the deepening of the trade wind layer [Nuijens and Stevens, 2012] and influence the observed cloud field properties. This possible influence is neglected in the current study.

### 6.3. Additional parameters

The previous chapters show that moisture and wind speed alone cannot explain observed cloud field patterns. Wind shear, vertical velocity, and the stability in the lower troposphere might play a role as well. They are therefore investigated in this chapter. For consistency, each variable discussed is accompanied by a frequency distribution and a figure showing all statistical measures used in the previous chapters to describe the observed cloud fields, similar to Figure 19 and Figure 22. However, they are not explained in detail. Instead, only relevant findings are noted.

#### 6.3.1. Wind shear

Wind speed and wind shear are known to be positively correlated [Brueck et al., 2015]. The changes in cloud field properties due to changes in wind speed might therefore include wind shear effects too. In the following, the role of wind shear is investigated by sorting the ASTER dataset according to increasing wind shear and deriving cloud properties similarly to Chapter 6.1 and Chapter 6.2.

Wind shear is defined as the absolute value of the wind vector difference between 700 hPa and 1000 hPa. It is derived from the ERA-interim dataset (see Chapter 3.3). Figure 23 shows the distribution of wind shear for the 1917 ASTER images. Sorting these images into bins of increasing wind shear results in no significant dependencies of cloud properties upon wind shear. From the literature, it is expected to find a higher cloud fraction and larger cloud sizes due to the tilting of clouds with increasing wind shear. Neggers et al. [2003] even show an increase in the scale break size with increasing wind shear based on an LES study. In the current study, although the scale break size slightly increases, the slope of the size distribution does not show a clear dependence on wind shear. The cloud fraction slightly increases, but is accompanied by a large uncertainty.

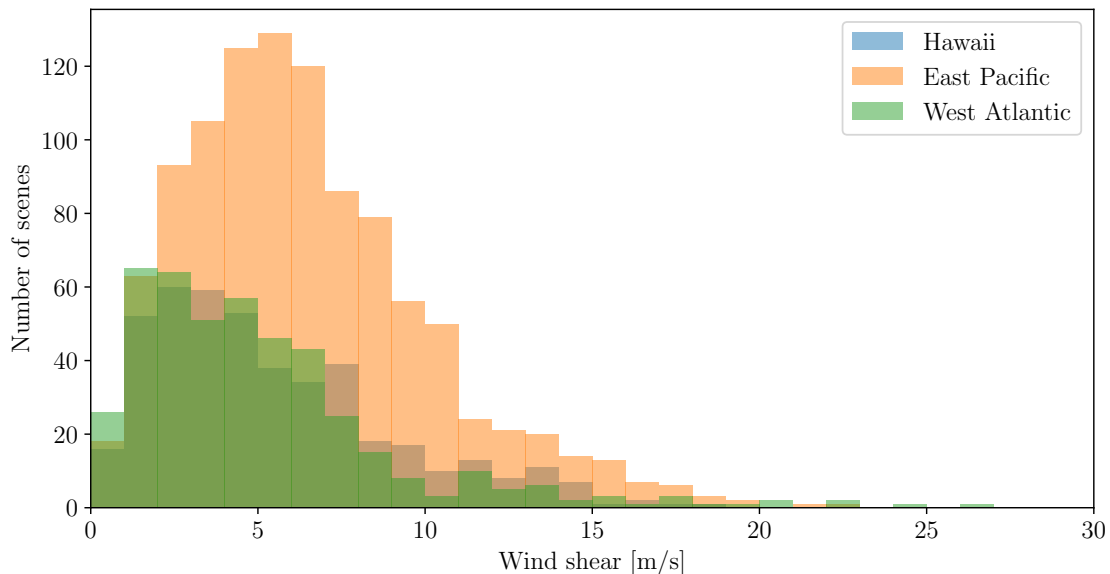


**Figure 23:** Distribution of scene-average wind shear calculated from ERA-interim wind speeds for 1917 ASTER images. The data is displayed separately for three different regions. Scenes located west of  $140^\circ$  W are displayed in blue ('Hawaii'), between  $140^\circ$  W and  $81^\circ$  W in orange ('East Pacific') and east of  $81^\circ$  W in green ('West Atlantic'). The bin width is  $1 \text{ m/s}$ .

Therefore, no clear relations can be drawn between wind shear and cloud properties. Wind shear within the cloud layer might be more relevant to direct cloud interactions and might lead to clearer findings. Nevertheless, an observational study by Brueck et al. [2015] and a modeling study by Nuijens et al. [2015] both suggest that wind shear plays a minor role in regulating cloud fields in the trade wind region.

### 6.3.2. Vertical velocity

Large-scale subsidence is one of the key features of the trade wind regions. Especially during the dry winter season, the trades are dominated by subsiding air masses, while deeper clouds are found during summer months under weak rising motion [Brueck et al., 2015]. In the following, it is evaluated to what extent vertical velocity controls cloud field properties in the trades.

Figure 25 shows the distribution of vertical velocity averaged over the cloud layer (850–600 hPa) for the 1917 ASTER images. Cloud fields are sampled over a large variety of conditions ranging from weak rising (negative values) to moderate subsiding motion (positive values).

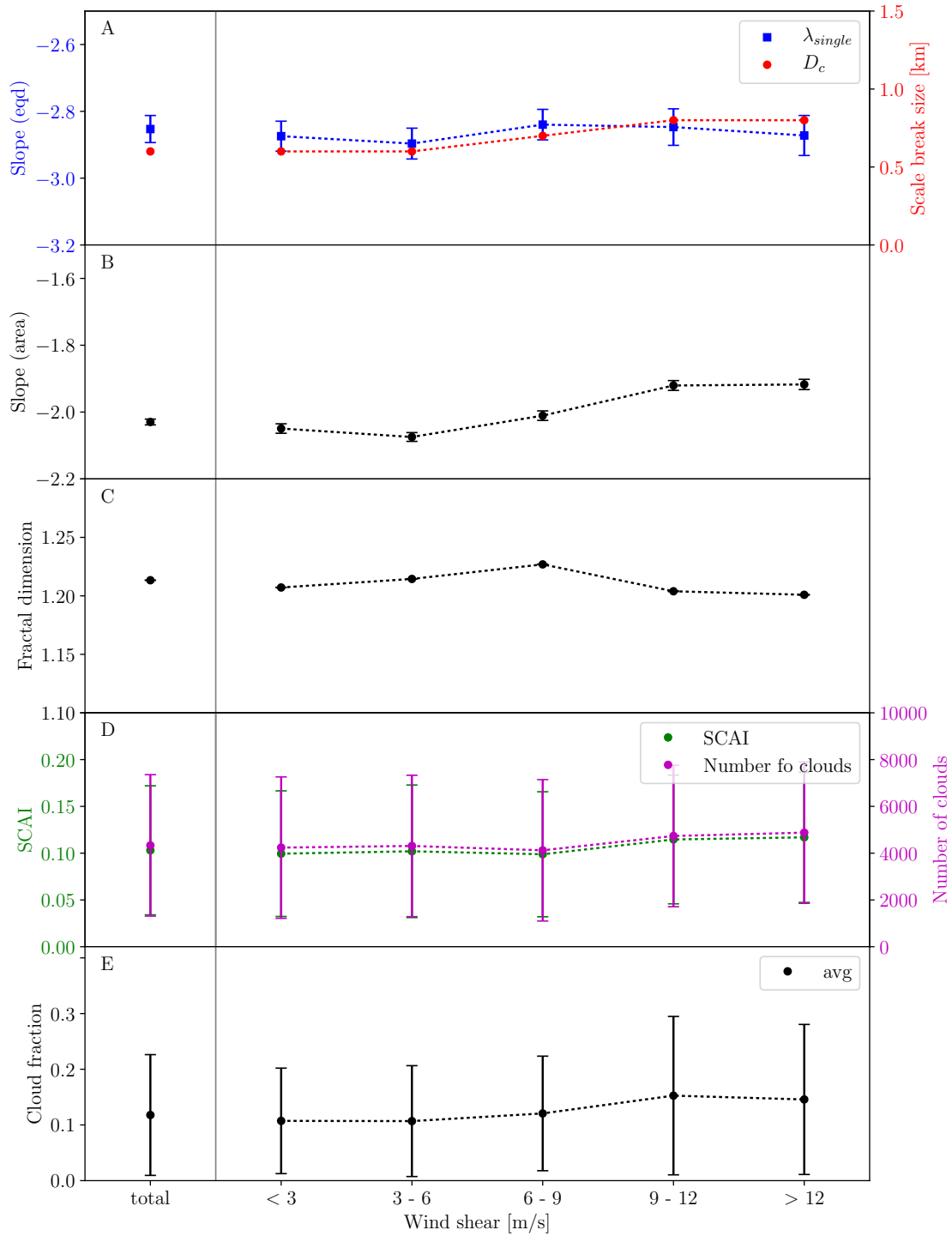


**Figure 24:** Cloud field properties as a function of surface wind speed. 1917 ASTER images are sorted into different bins according to the scene-average wind shear calculated from ERA-interim wind speeds. See the caption of Figure 19 for a full description of the parameters.

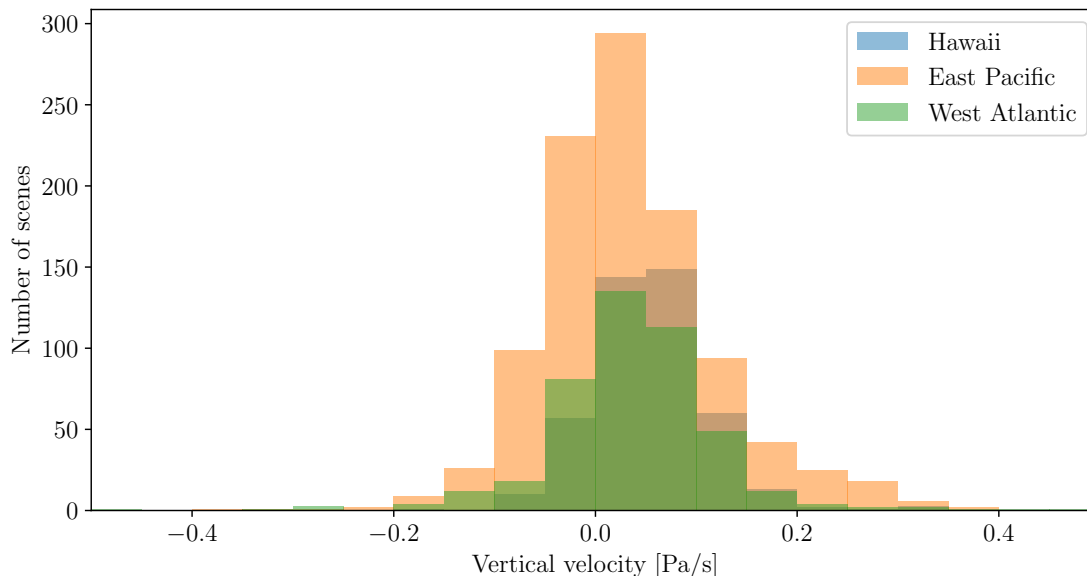


**Figure 25:** Distribution of scene-average vertical velocity from ERA-interim data for 1917 ASTER images. The data is displayed separately for three different regions. Scenes located west of  $140^\circ$  W are displayed in blue ('Hawaii'), between  $140^\circ$  W and  $81^\circ$  W in orange ('East Pacific') and east of  $81^\circ$  W in green ('West Atlantic'). The bin width is  $0.05 \text{ Pa/s}$ .

Figure 26 demonstrates that cloud field properties tend to be similar for strong rising and subsiding air masses. Starting from zero vertical velocity, clouds become larger (panel **A** and **B**) and the cloud fraction is slightly higher (although within the uncertainty range) with increasing as well as decreasing vertical velocity (panel **E**). In addition, the fractal dimension shows a pronounced development towards compact shapes under strong vertical motion (panel **C**).

At first sight, these results seem counterintuitive. However, Brueck et al. [2015] find similar relations concerning the cloud fraction from two years of cloud observations at the BCO and explain them with different processes acting in the trade wind layer for rising and subsiding motions. Strong subsidence stabilizes the trade wind layer, which leads to a lateral spreading of clouds at the strong inversion layer (see Chapter 6.3.3). Therefore, individual projected cloud areas, as well as the overall cloud fraction are larger in an ASTER image.

Larger clouds under rising motion might result from a combined effect of several variables. Brueck et al. [2015] observe that vertical velocity is highly correlated with relative humidity in the sub-cloud layer, temperature advection, and lower tropospheric stability. A warm, moist and unstable sub-cloud layer provides the potential for deeper and larger cumulus clouds to form. The stability of the lower troposphere is linked to vertical velocity and might also correlate with observed cloud field properties. Therefore, it is evaluated separately in the following chapter.

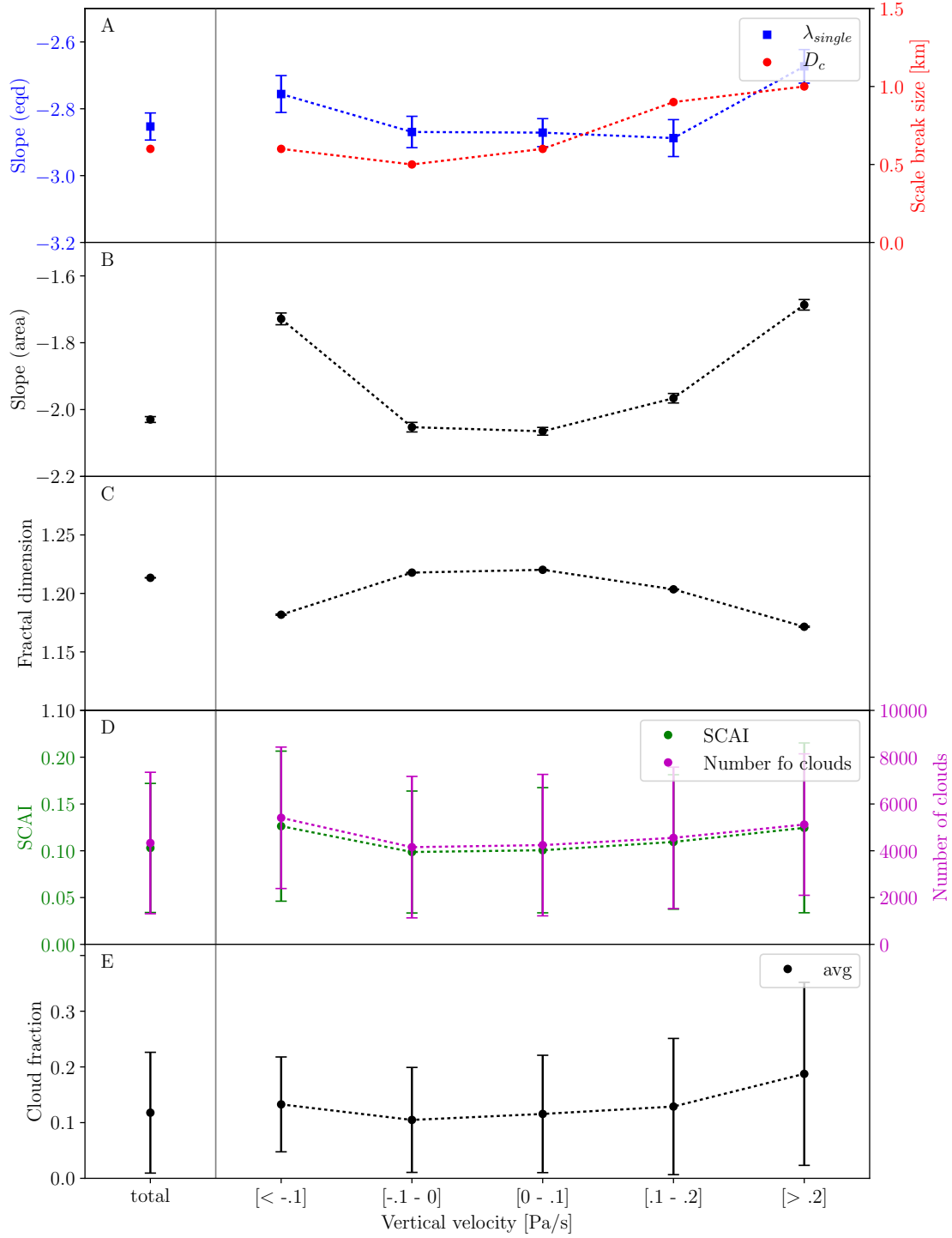


**Figure 26:** Cloud field properties as a function of surface wind speed. 1917 ASTER images are sorted into different bins according to the scene-average vertical velocity from ERA-interim averaged between 600 hPa and 850 hPa. See the caption of Figure 19 for a full description of the parameters.

### 6.3.3. Lower tropospheric stability

According to Wood and Bretherton [2006], the lower tropospheric stability (LTS) is highly correlated with the cloud fraction of stratiform low clouds in the subtropics. LTS is a measure of the strength of the capping inversion at the top of the trade wind boundary layer. It is defined as the difference in potential temperature between 700 hPa and the surface. Brueck et al. [2015] show that LTS correlates with the cloud fraction observed at the BCO where trade wind cumulus clouds dominate. To investigate the relationship between cloud fraction in the ASTER dataset and LTS, temperature values from ERA-interim reanalysis at 700 hPa and 1000 hPa are extracted and the corresponding potential temperatures, as well as their differences are calculated (see Chapter 3.3). Figure 28 panel **E** shows that the cloud fraction indeed increases with increasing stability, although staying within the uncertainty range defined by the standard deviation. Changes in the slope of the cloud size distribution (panel **A** and **B**), as well as in the scale break size (panel **A**), indicate the presence of larger clouds in stable situations. This is consistent with the idea that an increase in stability leads to a lateral expansion of clouds at the inversion layer. However, these relationships are characterized by high uncertainties. Brueck et al. [2015] propose from observing seasonal variations in the relationship of cloudiness and LTS that the latter might be a limiting, but no controlling factor to shallow cumulus clouds in the trades. It is also hypothesized in their study that LTS cannot be considered alone, but rather needs to be put within the context of large-scale dynamics.

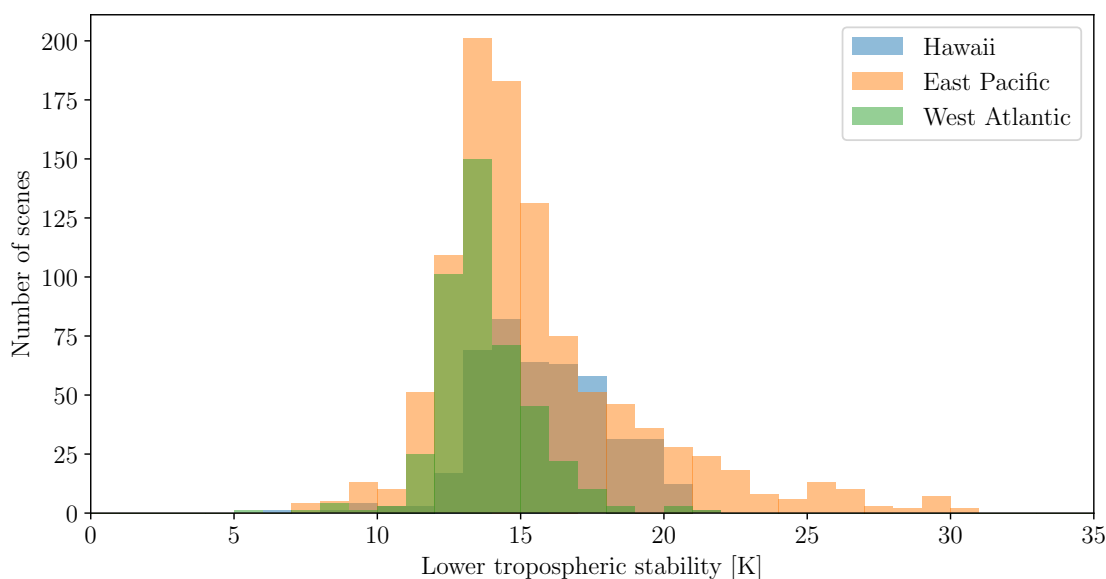


**Figure 27:** Distribution of scene-average lower tropospheric stability (LTS) calculated from ERA-interim temperatures for 1917 ASTER images. The data is displayed separately for three different regions. Scenes located west of 140° W are displayed in blue ('Hawaii'), between 140° W and 81° W in orange ('East Pacific') and east of 81° W in green ('West Atlantic'). The bin width is 1 K.

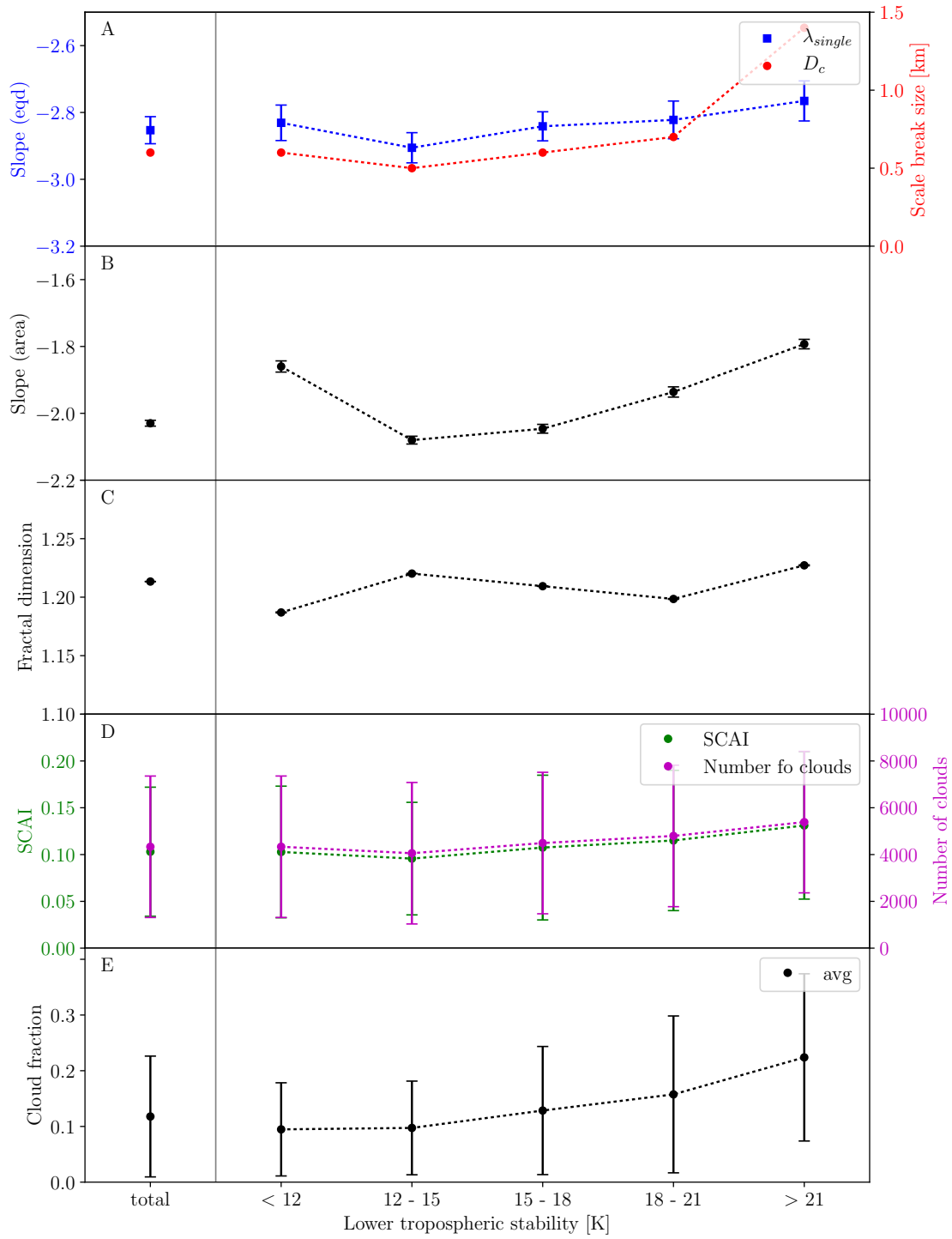


**Figure 28:** Cloud field properties as a function of lower tropospheric stability (LTS). 1917 ASTER images are sorted into different bins according to the scene-average LTS calculated from ERA-interim temperatures. See the caption of Figure 19 for a full description of the parameters.

## 6.4. Cloud feedback in a warming climate

In studies of climate change, the change in cloud fraction is always present due to the various feedbacks related to it, such as interaction of clouds and radiation and the radiation budget. State of the art climate models show a remarkable spread in the reaction to warming of low-level cloudiness in the trades. Bretherton [2015] reports a negative cloud feedback for trade wind cumuli in a warming climate meaning that the low level cloud cover is reduced. Similarly, Vogel et al. [2016] find that trade wind cumuli respond to climate warming with a decrease in cloud cover using LES simulations. Brient et al. [2015] suggest from a global model inter-comparison study a decrease in low-level cloud fraction due to convective drying and deepening of shallow clouds.

The ASTER dataset is not suited for a climate study. However, from analyzing regions with higher and lower SST in present day climate, one can attempt to investigate the response of clouds to warming. When sorting the ASTER images according to increasing SST the cloud fraction decreases on average (see Figure 30). This supports the idea of a negative low cloud feedback for shallow cumulus clouds in the trades to warming. The same negative correlation of SST and low-level cloudiness was found by Stein et al. [2017]. In addition, cloud fields corresponding to warmer ocean surfaces have a cloud size distribution indicating a relatively larger number of small clouds, while the total number of clouds stays constant (see Figure 30). Furthermore, cloud fields seem to be more aggregated (lower SCAI) with higher SST. Reasons for and implications from this relation, however, are subject of ongoing investigations. The binning according to different SSTs might at the same time imply a strong regional sampling as ocean currents also influence SST. A more detailed analysis is needed, which is beyond the scope of this work.

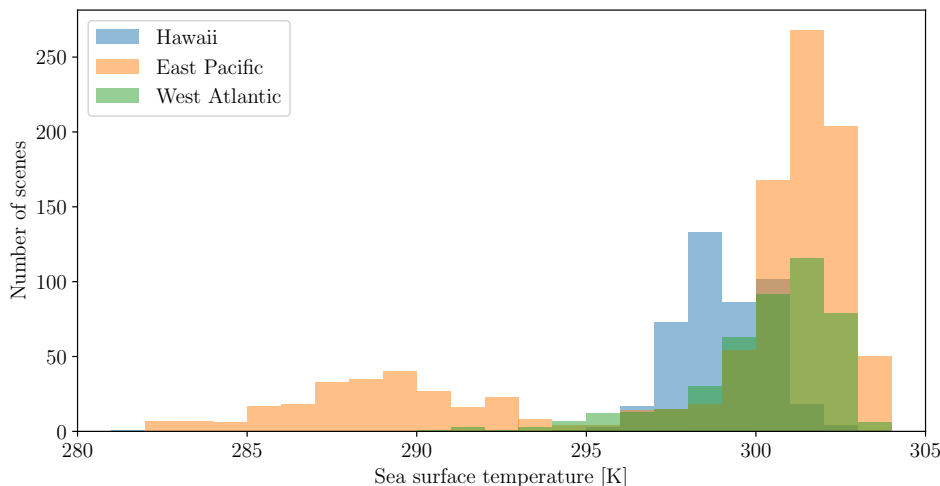


**Figure 29:** Distribution of scene-average sea surface temperature (SST) from ERA-interim for 1917 ASTER images. The data is displayed separately for three different regions. Scenes located west of  $140^{\circ}$  W are displayed in blue ('Hawaii'), between  $140^{\circ}$  W and  $81^{\circ}$  W in orange ('East Pacific') and east of  $81^{\circ}$  W in green ('West Atlantic'). The bin width is 1 K.

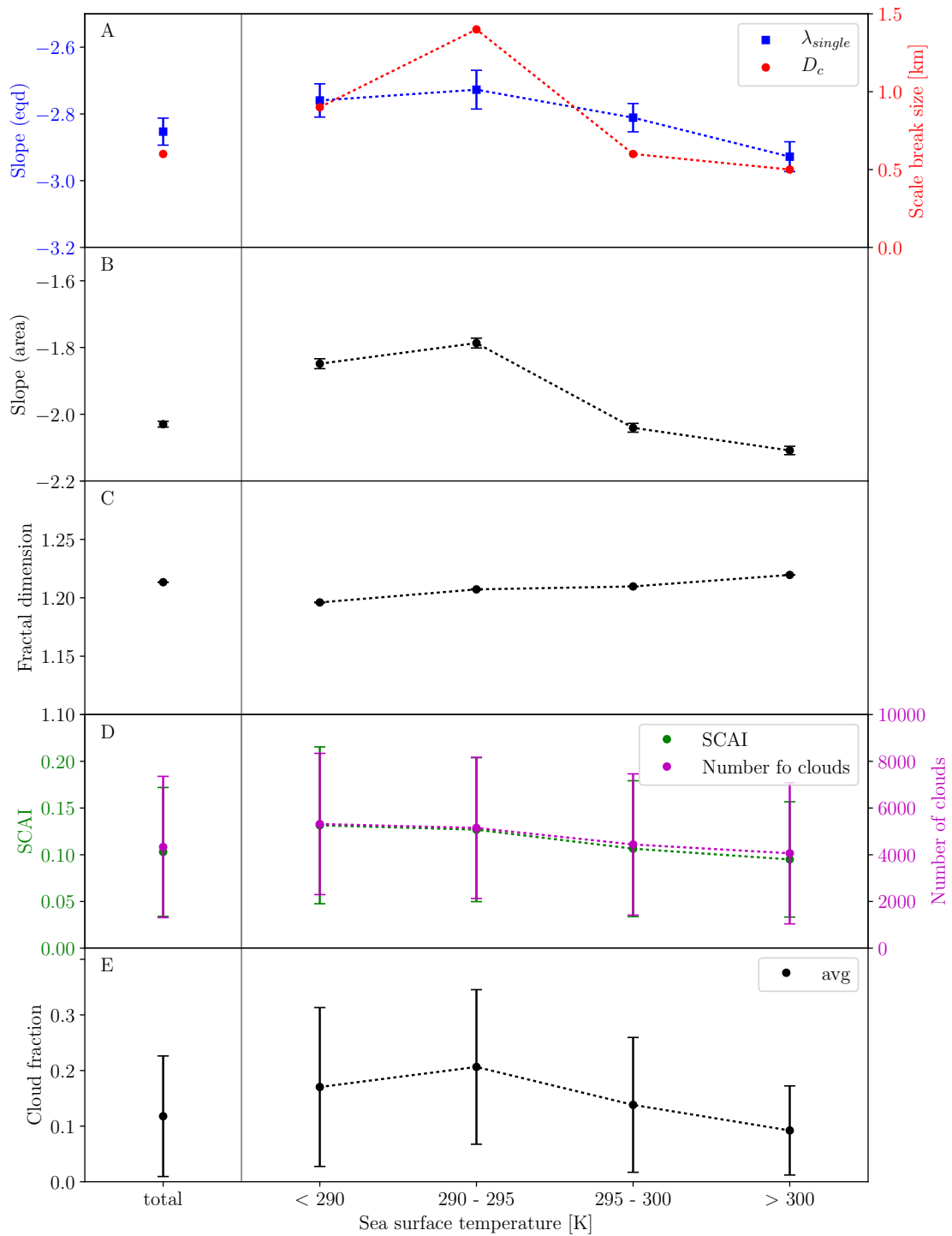


**Figure 30:** Cloud field properties as a function of sea surface temperature (SST). 1917 ASTER images are sorted into different bins according to the scene-average SST from ERA-interim reanalysis. See the caption of Figure 19 for a full description of the parameters.

## 7. Limitations of the study

This study is subject to some restrictions. In the following chapter, the four major limitations are discussed that arise from the ASTER datasets and from the subjective decisions made when creating the cloud mask and defining individual cloud entities, followed by the evaluation whether supplementary data from MODIS and ERA-interim are convenient to use.

The first and most relevant limitation to this study is the scarce availability of cloudy ASTER images. This limits a spatially consistent monitoring of shallow cumulus clouds and makes a climatological view difficult. Nevertheless, an ASTER dataset was constructed of a large number of images that fulfill the conditions stated in Chapter 4.1. The subjectively defined conditions aim to extract images showing exclusively shallow cumulus clouds to evaluate the question whether universal properties characterizing such cloud fields exist. Many studies on low level clouds in the trades also consider stratocumulus clouds. A direct comparison of cloud properties, such as the cloud fraction, with these studies might be affected by this. However, such findings from the literature provide ideas on possible methodological and physical relations connected to trade wind cumulus cloud fields.

Furthermore, finding an appropriate cloud mask is a challenging task. The classification of pixels as either clear or cloudy provides the basis for calculating macrophysical cloud properties. The cloud masking algorithm of Werner et al. [2016] serves the purpose of this study well in detecting small and shallow trade wind cumulus clouds over the tropical ocean. Within the thresholding tests, it was decided to ease one condition to allow the derivation of a cloud mask under conditions of strong sun glint too. Every single cloud mask was visually checked confirming that this change in the algorithm does not reduce the quality of the cloud masks but simply increases the number of samples in the dataset.

Cloud masks from 105 ASTER images recorded during the RICO campaign were validated against those manually derived by Zhao and Di Girolamo [2007]. Cloud properties calculated from the two different cloud masks are in good agreement (see Figures in Appendix A.1). In addition, some studies that use cloud masks exclude clusters touching the domain boundaries because they exhibit unphysical shapes. In the current study, such clouds are not excluded. However, trade wind cumulus clouds have small sizes and the qualitative results found in this study are expected to be insensitive to that choice.

Due to the choice of the 4-connectivity rule in the cloud detection process one might question the universality of the results. Some statistical measures are expected to change quantitatively when using the 8-connectivity rule. Most obviously, the number of detected clouds will be smaller. Nevertheless, the results are expected to be independent of this choice in a qualitative sense.

Zhao and Di Girolamo [2007] argue that cloud size distribution as well as the cloud spatial distribution are insensitive to the exact definition of the cloud edge. And in particular, the cloud fraction and cloud top height do not depend on the segmentation used.

Concerning the investigation of controlling parameters to cloud field properties, several factors introduce uncertainty in the found relationships. First of all, meteorological variables, such as total column water vapor from MODIS as well as other parameters from ERA-interim reanalysis, have retrieval uncertainties. In addition, ERA-interim has an analysis output every 6 hours leading to a maximum temporal difference of up to 3 hours to the ASTER observation in time. Assuming an average wind speed of 5 m/s air parcels move about 50 km within 3 hours, which matches the ASTER domain size. The meteorological variables can therefore be considered to give an adequate description of the local conditions corresponding to observed cloud fields. A factor complicating the interpretation of the results is introduced by including ASTER images collected over the North Pacific at higher latitudes. Some meteorological variables, such as total column water vapor and sea surface temperature, show considerably different values suggesting that different physical and dynamical processes might act there compared to the typical trade wind region. However, the main findings summarized in the following chapter are in agreement with findings from previous studies.

## 8. Conclusions and outlook

The current work investigates 1917 ASTER images collected over the tropical and sub-tropical Atlantic and Pacific ocean during the years 2000 to 2007. This comprehensive dataset consists of images showing exclusively shallow cumulus clouds. The high spatial resolution of the ASTER bands provides the potential to investigate such small clouds, which are known to exhibit cloud sizes smaller than 1 km in diameter [Zhao and Di Girolamo, 2007].

The study aims to derive cloud field properties of cumulus clouds in the trade wind boundary layer. Therefore, a sophisticated cloud masking algorithm following Werner et al. [2016] is applied to construct cloud masks as a basis for further statistical calculations. Considering all 1917 cloud fields results in an average cloud fraction of 11.8 % with individual scene values ranging between 0 and 40 %. This is in agreement with previous studies. Zhao and Di Girolamo [2007] find an average value of 8.6 % while other studies report higher values [Brueck et al., 2015]. The cloud top height (CTH) was calculated using the infrared-window method similar to the calculation of the MODIS Collection 6 cloud top properties. Brightness temperatures from the ASTER thermal band at 11  $\mu\text{m}$  are used in combination with latitude-dependent apparent lapse rates to calculate CTHs. The distribution of scene average CTHs exhibits a peak at 1 km and the overall average CTH is about 1.2 km. A clear second peak in the distribution is not found, which is in disagreement with the bimodal distribution observed by Genkova et al. [2007]. However, their study includes deeper convective clouds that are explicitly excluded from the current study.

The ensemble of cloud shapes is characterized by the cloud size distribution and the fractal dimension. Assuming a single power law, the distribution of cloud equivalent diameters can be fitted on a logarithmic scale with a slope of -2.85. For a double power law fit a characteristic scale break at 600 m is found. Fitting the size distribution of cloud areas instead, results in a slope close to the one predicted by two-dimensional critical percolation theory. This suggests that the shape of the cloud area distribution is a robust geometrical feature allowing for only slight variations due to physical processes. For the fractal dimension a value of 1.21 is found indicating that the sampled clouds are rather compact and with smoother shapes compared to former studies which report higher values. However, the value is relatively close to the frequently proposed value of  $\frac{4}{3}$  (Cahalan and Joseph [1989], Benner et al. [1998], Peters et al. [2009]) and shows to be a very robust measure throughout this study.

The analysis of the cloud spatial distribution reveals that trade wind cumulus clouds appear more frequently in the form of aggregated cloud fields. Clouds show small nearest neighbor distances most frequently within 50–100 m. Next to the distance in between clouds, the total number within each ASTER image also characterizes

the aggregation state. Tobin et al. [2012] introduced the SCAI index, a combined measure of distance and number of clouds for deep convection. In the current study the average SCAI amounts to 0.1, which is in agreement with findings from Stein et al. [2017]. Summarizing, observed cloud field properties from ASTER images are within reasonable ranges and largely consistent with previous studies.

The second part of this work evaluates the relationship between large-scale meteorological conditions and cloud field properties. Moisture in the lower troposphere and the height of the trade wind boundary layer were suggested as major controlling factors. Concerning moisture, it was found that larger clouds are observed under both, very dry and very moist conditions. The former result is somewhat counterintuitive and puzzling. The cloud fraction tends to decrease with increasing moisture confirming findings from Brueck et al. [2015].

Variations in the trade wind boundary layer height are approximated from a change in the average cloud top height. Cloud top heights are shown to be strongly correlated with surface wind speeds (Nuijens et al. [2014] and Brueck et al. [2015]). Based on previous studies a hypothesis is defined such that with increasing wind speed the trade wind layer deepens leading to cumulus clouds with higher cloud tops. The deepening is associated with larger clouds, depicted by a less steep slope in the cloud size distribution, and a higher cloud fraction. This hypothesis is confirmed by the analysis and, in addition, cloud fields appear to be more aggregated at lower wind speeds.

Wind speed and moisture alone cannot fully explain the variability seen in cloud field properties. Observed changes are likely to be caused by a combination of several covarying meteorological variables. Wind shear is investigated and it seems to be of minor importance. Nevertheless, in a situation with strong wind speed and deeper clouds, significant wind shear can lead to clouds with larger projected areas and, thus, a slight increase in cloud fraction due to the tilting of clouds as proposed by Neggers et al. [2003]. Large-scale vertical motion is one of the key features in the trade wind region and it is providing the frame for shallow cumulus clouds observed. It is interesting to find similar cloud field properties for both, the typical subsiding, as well as the less frequent rising motion. Larger and more compact clouds and a higher cloud fraction can be explained for both situations with different physical and dynamical processes acting in the trade wind boundary layer. Similar results are stated in Brueck et al. [2015].

The stability of the lower troposphere is strongly connected to the vertical velocity. In very stable situations clouds tend to be larger and consequently cloud fraction increases. However, the relation is weak in the data suggesting that stability is not a major controlling factor. A negative correlation is found between cloud fraction and sea surface temperature suggesting a low climate sensitivity of shallow cumulus clouds to climate warming. This statement is based on a very simplified relation of

the occurrence of shallow clouds over areas of different sea surface temperatures. However, recent studies from Brient et al. [2015] and Vogel et al. [2016] similarly find a decrease in low level cloud cover in a warmer climate.

This study lends observational evidence to some of the proposed control mechanisms of trade wind cumulus clouds. However, it also demonstrates the incomplete understanding of the underlying physical processes and dynamical interactions of the observed clouds with their environment. None of the analyzed large-scale meteorological variables stands out alone as the main driver of observed cloud field properties. The covariance of these parameters is a further complicating factor. Therefore, it is proposed to compare cloud field properties to physical processes that are described by a combination of controlling variables rather than comparing them to single variables. Observations showed for example that strong surface winds can lead to deeper clouds, whereas large-scale subsidence and a stable lower troposphere can dampen the deepening so that the overall effect is a horizontal spreading of clouds instead. Considering processes might provide more insight into the topic.

Furthermore, total column water vapor was used in this study to characterize moisture, but other measures might be more appropriate. In high-resolution ICON LES simulations similar spatial patterns can be observed in shallow cumulus cloud fields and the surface relative humidity in the tropics [Matthias Brück, personal communication, June 2017]. This implies that relative humidity at the surface has a strong influence on the development and organization of the cloud field. Further studies are needed to characterize the relationship between cloud field properties and meteorological parameters that are not investigated in the current work (e.g. Bowen ratio, surface relative humidity). Understanding control parameters and processes more accurately can improve convective parametrization schemes in cloud resolving models and large-eddy simulations and eventually reduce some uncertainty in climate projections.

## A. Appendix A

### A.1. Cloud mask

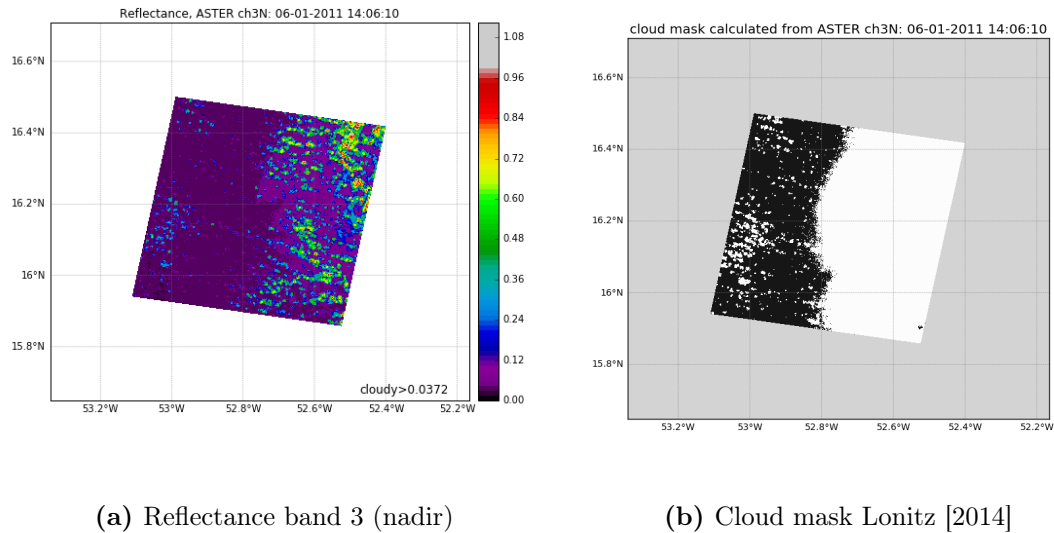


**Figure 31:** ASTER images recorded on the 6<sup>th</sup> of January 2011, 14:06:10 UTC over the West Atlantic. In (a) a false-color image of band 3 (nadir,  $0.86 \mu\text{m}$ ) of reflectance values is shown and (b) is the corresponding cloud mask calculated according to Lonitz [2014].

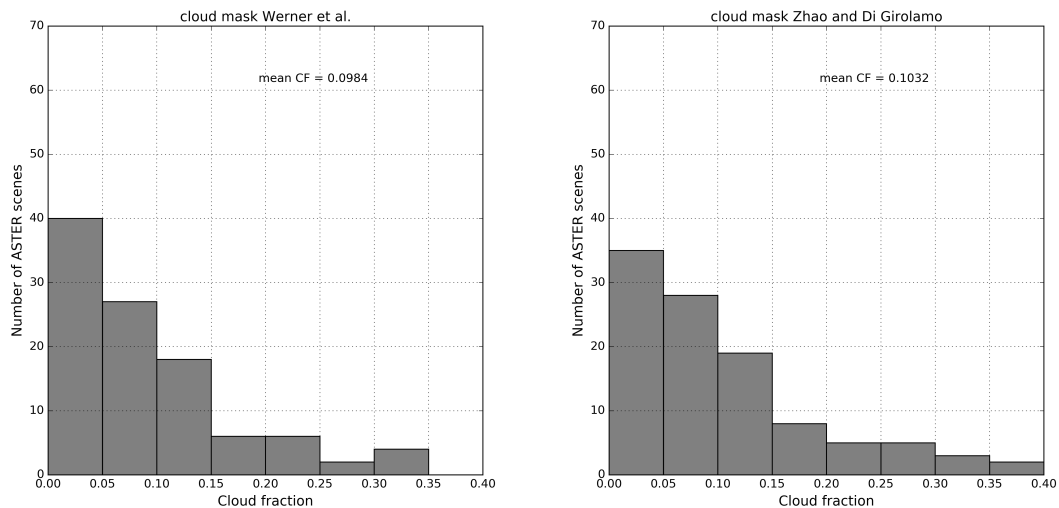


**Figure 32:** Frequency distributions of cloud fraction in 105 ASTER images collected during the RICO campaign in 2004. The distributions are based on two different cloud masking schemes, one according to Werner et al. [2016] (left) and the other according to Zhao and Di Girolamo [2007] (right).

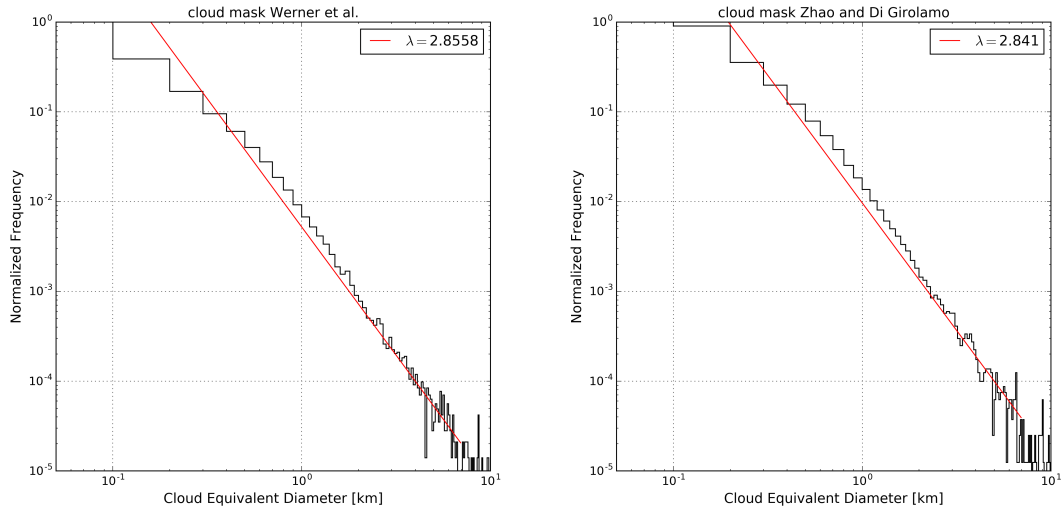


**Figure 33:** Cloud size distributions from 105 ASTER images collected during the RICO campaign in 2004. The distributions are based on two different cloud masking schemes, one according to Werner et al. [2016] (left) and the other according to Zhao and Di Girolamo [2007] (right).

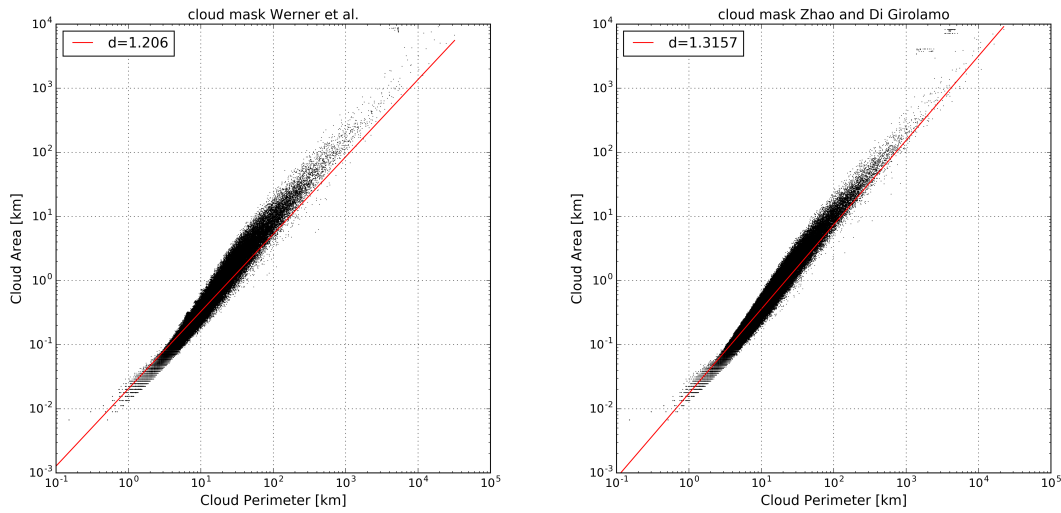


**Figure 34:** Scatter plot of cloud equivalent diameters and cloud perimeter and the derived fractal dimensions from 105 ASTER images collected during the RICO campaign in 2004. The calculations of cloud area and cloud perimeter are based on two different cloud masking schemes, one according to Werner et al. [2016] (left) and the other according to Zhao and Di Girolamo [2007] (right).

## A.2. Cloud properties

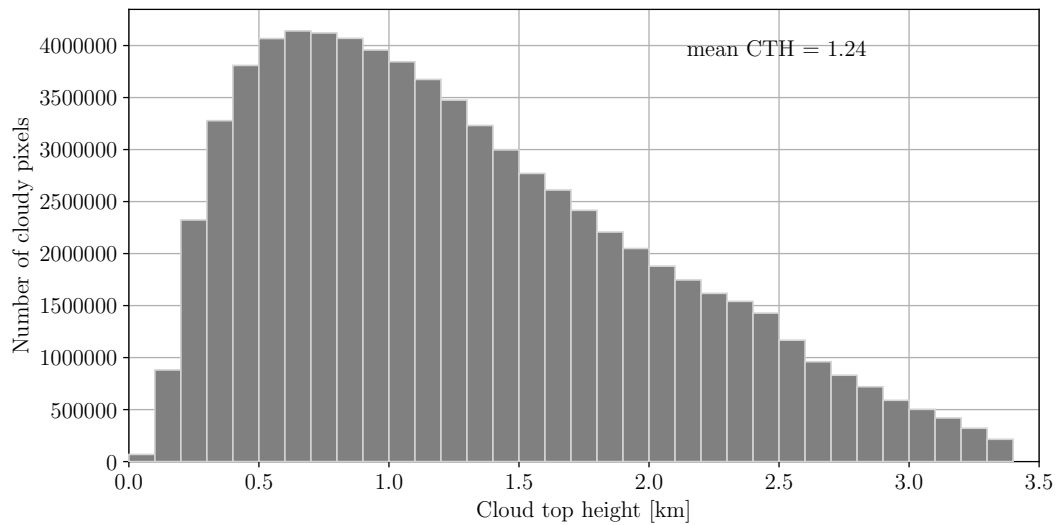


**Figure 35:** Frequency distribution of cloud top heights from fully cloudy TIR pixels in 1917 ASTER images. The bin width is 100 m.

## A.3. TCWV from ERA-interim

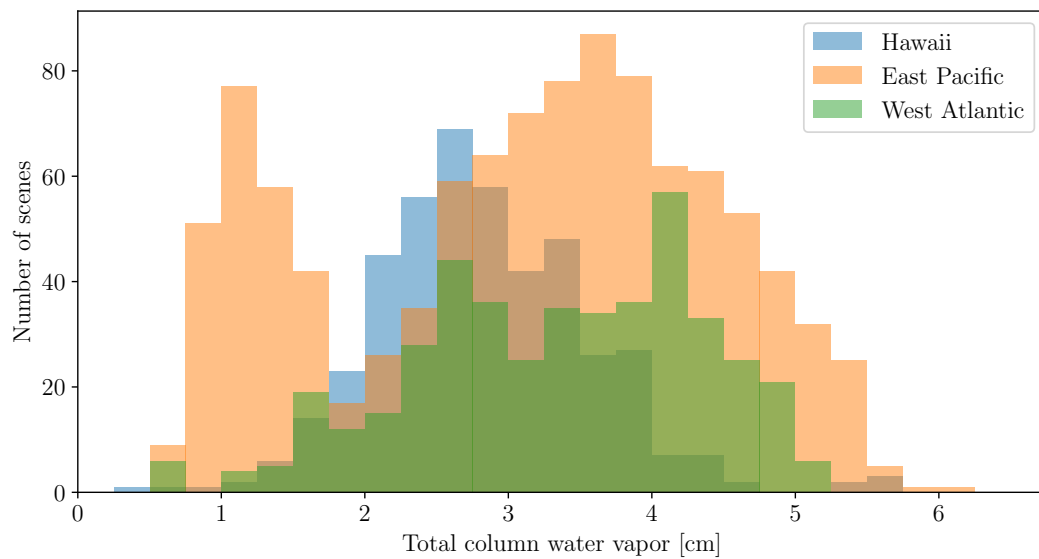


**Figure 36:** Distribution of scene-average total column water vapor (TCWV) from ERA-interim reanalysis corresponding to the 1917 ASTER images. The data is displayed separately for three different regions. Scenes located west of  $140^\circ$  W are displayed in blue ('Hawaii'), between  $140^\circ$  W and  $81^\circ$  W in orange ('East Pacific') and east of  $81^\circ$  W in green ('West Atlantic'). The bin width is 0.25 cm.

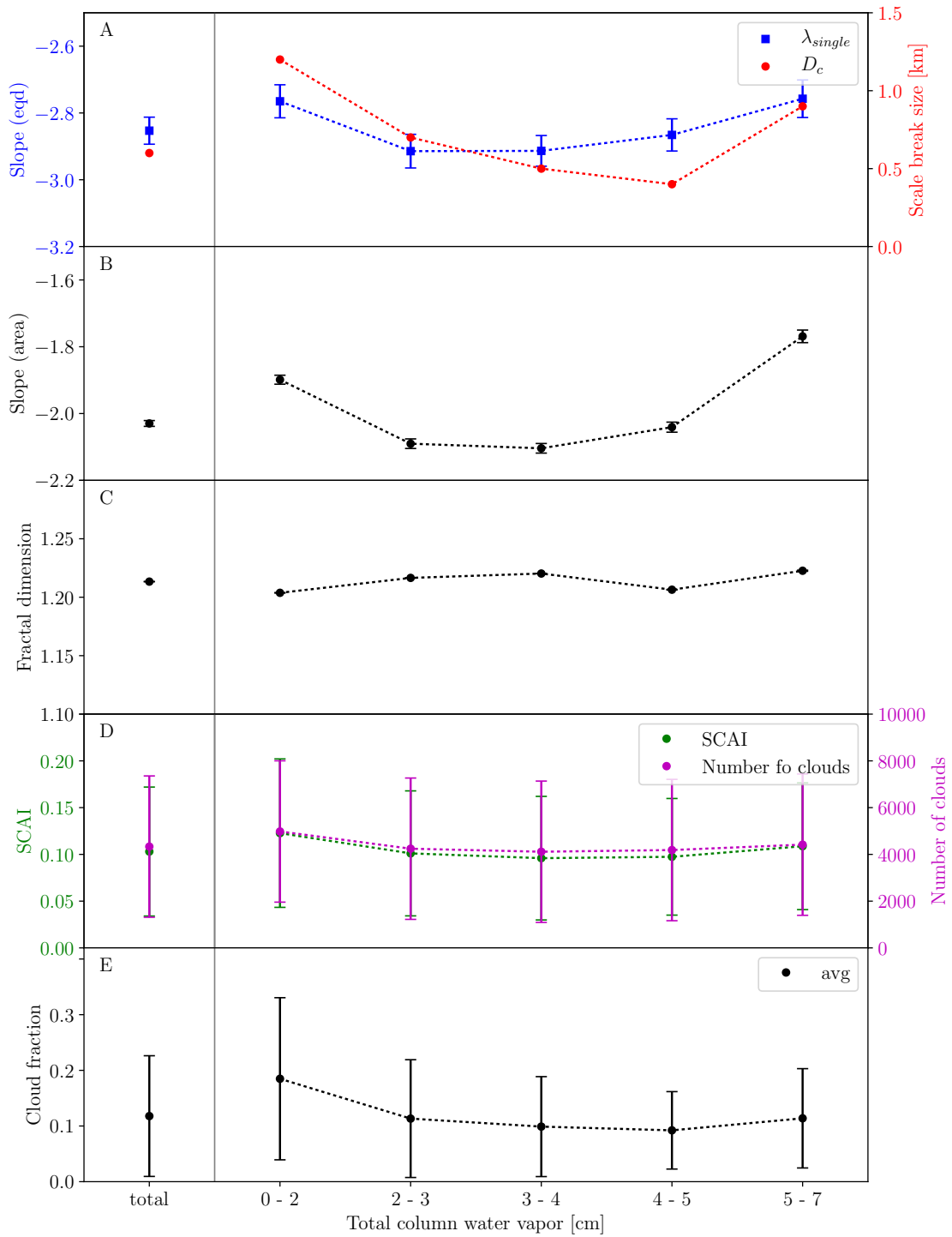


**Figure 37:** Cloud field properties as a function of total column water vapor (TCWV). 1917 ASTER images are sorted into different bins according to the scene-average TCWV from ERA-interim reanalysis. See the caption of Figure 19 for a full description of the parameters.

## Acronyms

**ACCAA** ASTER Cloud Coverage Assessment Algorithm.

**ASTER** Advanced Spaceborne Thermal Emission and Reflection Radiometer.

**BCO** Barbados Cloud Observatory.

**CTH** cloud top height.

**ECMWF** European Centre for Medium-Range Weather Forecasts.

**ERA-interim** global atmospheric European reanalysis dataset.

**ITCZ** Inter-Tropical-Convergence Zone.

**LES** Large-eddy simulation.

**LTS** Lower Tropospheric Stability.

**MCS** Mesoscale Convective System.

**MODIS** Moderate-resolution Imaging Spectroradiometer.

**NARVAL** Next-Generation Airborne Remote Sensing for Validation Studies.

**NASA** National Aeronautics and Space Administration.

**RICO** Rain In Cumulus over the Ocean.

**SCAI** Simple Convective Aggregation Index.

**SST** sea surface temperature.

**SWIR** shortwave infrared.

**TCWV** total column water vapor.

**TIR** thermal infrared.

**TOA** top of atmosphere.

**UCC** unit conversion coefficient.

**VNIR** visible and near-infrared.

## References

- Bryan A. Baum, W. Paul Menzel, Richard A. Frey, David C. Tobin, Robert E. Holz, Steve A. Ackerman, Andrew K. Heidinger, and Ping Yang. Modis cloud-top property refinements for collection 6. *Journal of Applied Meteorology and Climatology*, 51(6):1145–1163, 2012. doi: 10.1175/JAMC-D-11-0203.1. URL <http://dx.doi.org/10.1175/JAMC-D-11-0203.1>.
- T. C. Benner, J. A. Curry, and P. J. Webster. Characteristics of small tropical cumulus clouds and their impact on the environment. *J. Geoph. Res.*, page 2875328767, 1998.
- P. Berrisford, D.P. Dee, P. Poli, R. Brugge, K. Fielding, M. Fuentes, P.W. Källberg, S. Kobayashi, S. Uppala, and A. Simmons. The era-interim archive version 2.0. Shinfield Park, Reading, November 2011.
- Sandrine Bony, Bjorn Stevens, Dargan M. W. Frierson, Christian Jakob, Masa Kageyama, Robert Pincus, Theodore G. Shepherd, Steven C. Sherwood, A. Pier Siebesma, Adam H. Sobel, Masahiro Watanabe, and Mark J. Webb. Clouds, circulation and climate sensitivity. *Nature Geoscience*, 8(4):261–268, March 2015. ISSN 1752-0894. doi: 10.1038/ngeo2398. URL <http://dx.doi.org/10.1038/ngeo2398>.
- Christopher S. Bretherton. Insights into low-latitude cloud feedbacks from high-resolution models. *Philosophical Transactions of the Royal Society of London A: Mathematical, Physical and Engineering Sciences*, 373(2054), 2015. ISSN 1364-503X. doi: 10.1098/rsta.2014.0415. URL <http://rsta.royalsocietypublishing.org/content/373/2054/20140415>.
- Florent Brient, Tapio Schneider, Zhihong Tan, Sandrine Bony, Xin Qu, and Alex Hall. Shallowness of tropical low clouds as a predictor of climate models’ response to warming. *Climate Dynamics*, pages 1–17, 2015. ISSN 1432-0894. doi: 10.1007/s00382-015-2846-0. URL <http://dx.doi.org/10.1007/s00382-015-2846-0>.
- Matthias Brueck, Louise Nuijens, and Bjorn Stevens. On the seasonal and synoptic time-scale variability of the north atlantic trade wind region and its low-level clouds. *Journal of the Atmospheric Sciences*, 72(4):1428–1446, 2015. doi: 10.1175/JAS-D-14-0054.1. URL <http://dx.doi.org/10.1175/JAS-D-14-0054.1>.
- Robert F. Cahalan and Joachim H. Joseph. Fractal statistics of cloud fields. *Monthly Weather Review*, 117(2):261–272, 1989. doi: 10.1175/1520-0493(1989)117<0261:FSOCF>2.0.CO;2. URL [http://dx.doi.org/10.1175/1520-0493\(1989\)117<0261:FSOCF>2.0.CO;2](http://dx.doi.org/10.1175/1520-0493(1989)117<0261:FSOCF>2.0.CO;2).
- D. P. Dee, S. M. Uppala, A. J. Simmons, P. Berrisford, P. Poli, S. Kobayashi, U. Andrae, M. A. Balmaseda, G. Balsamo, P. Bauer, P. Bechtold, A. C. M. Beljaars, L. van de Berg, J. Bidlot, N. Bormann, C. Delsol, R. Dragani, M. Fuentes,

- A. J. Geer, L. Haimberger, S. B. Healy, H. Hersbach, E. V. Hólm, L. Isaksen, P. Kållberg, M. Köhler, M. Matricardi, A. P. McNally, B. M. Monge-Sanz, J.-J. Morcrette, B.-K. Park, C. Peubey, P. de Rosnay, C. Tavalato, J.-N. Thépaut, and F. Vitart. The era-interim reanalysis: configuration and performance of the data assimilation system. *Quarterly Journal of the Royal Meteorological Society*, 137(656):553–597, 2011. ISSN 1477-870X. doi: 10.1002/qj.828. URL <http://dx.doi.org/10.1002/qj.828>.
- Iliana Genkova, Gabriela Seiz, Paquita Zuidema, Guangyu Zhao, and Larry Di Girolamo. Cloud top height comparisons from aster, misr, and {MODIS} for trade wind cumuli. *Remote Sensing of Environment*, 107(1–2):211 – 222, 2007. ISSN 0034-4257. doi: <https://doi.org/10.1016/j.rse.2006.07.021>. URL <http://www.sciencedirect.com/science/article/pii/S0034425706004421>. Multi-angle Imaging SpectroRadiometer (MISR) Special IssueMISR Special Issue.
- T. Heus and A. Seifert. Automated tracking of shallow cumulus clouds in large domain, long duration large eddy simulations. *Geoscientific Model Development*, 6(4):1261–1273, 2013. doi: 10.5194/gmd-6-1261-2013. URL <http://www.geosci-model-dev.net/6/1261/2013/>.
- G. C. Hulley and S. J. Hook. A new methodology for cloud detection and classification with aster data. *Geophysical Research Letters*, 35(16):n/a–n/a, 2008. ISSN 1944-8007. doi: 10.1029/2008GL034644. URL <http://dx.doi.org/10.1029/2008GL034644>. L16812.
- The Scikit image development team. skimage 0.14dev docs, 2017. URL <http://scikit-image.org/docs/dev/api/skimage.measure.html?highlight=regionprops#skimage.measure.label>.
- M. D. King, W. P. Menzel, Y. J. Kaufman, D. Tanre, Bo-Cai Gao, S. Platnick, S. A. Ackerman, L. A. Remer, R. Pincus, and P. A. Hubanks. Cloud and aerosol properties, precipitable water, and profiles of temperature and water vapor from modis. *IEEE Transactions on Geoscience and Remote Sensing*, 41(2):442–458, Feb 2003. ISSN 0196-2892. doi: 10.1109/TGRS.2002.808226.
- Katrin Lonitz. *Susceptibility of trade wind cumulus clouds to precipitation*. PhD thesis, Universität Hamburg, 2014.
- S. Lovejoy. Area-perimeter relation for rain and cloud areas. *Science*, 216(4542):185–187, 1982. ISSN 0036-8075. doi: 10.1126/science.216.4542.185. URL <http://science.sciencemag.org/content/216/4542/185>.
- Raúl Erlando López. The lognormal distribution and cumulus cloud populations. *Monthly Weather Review*, 105(7):865–872, 1977. doi: 10.1175/1520-0493(1977)105<0865:TLDACC>2.0.CO;2. URL [http://dx.doi.org/10.1175/1520-0493\(1977\)105<0865:TLDACC>2.0.CO;2](http://dx.doi.org/10.1175/1520-0493(1977)105<0865:TLDACC>2.0.CO;2).

- S. Hook M. Abrams and B. Ramachandran. *ASTER User Handbook Version 2*. Jet Propulsion Laboratory, 4800 Oak Grove Dr., Pasadena, CA 91109 and, 2002. URL [https://asterweb.jpl.nasa.gov/content/03\\_data/04\\_Documents/aster\\_user\\_guide\\_v2.pdf](https://asterweb.jpl.nasa.gov/content/03_data/04_Documents/aster_user_guide_v2.pdf).
- R. A. J. Neggers, H. J. J. Jonker, and A. P. Siebesma. Size statistics of cumulus cloud populations in large-eddy simulations. *Journal of the Atmospheric Sciences*, 60(8):1060–1074, 2003. doi: 10.1175/1520-0469(2003)60<1060:SSOCCP>2.0.CO;2. URL [http://dx.doi.org/10.1175/1520-0469\(2003\)60<1060:SSOCCP>2.0.CO;2](http://dx.doi.org/10.1175/1520-0469(2003)60<1060:SSOCCP>2.0.CO;2).
- L. Nuijens, I. Serikov, L. Hirsch, K. Lonitz, and B. Stevens. The distribution and variability of low-level cloud in the north atlantic trades. *Quarterly Journal of the Royal Meteorological Society*, 140(684):2364–2374, 2014. ISSN 1477-870X. doi: 10.1002/qj.2307. URL <http://dx.doi.org/10.1002/qj.2307>.
- Louise Nuijens and Bjorn Stevens. The influence of wind speed on shallow marine cumulus convection. *Journal of the Atmospheric Sciences*, 69(1):168–184, 2012. doi: 10.1175/JAS-D-11-02.1. URL <http://dx.doi.org/10.1175/JAS-D-11-02.1>.
- Louise Nuijens, Bjorn Stevens, and A. Pier Siebesma. The environment of precipitating shallow cumulus convection. *Journal of the Atmospheric Sciences*, 66(7):1962–1979, 2009. doi: 10.1175/2008JAS2841.1. URL <http://dx.doi.org/10.1175/2008JAS2841.1>.
- Louise Nuijens, Brian Medeiros, Irina Sandu, and Maike Ahlgrimm. Observed and modeled patterns of covariability between low-level cloudiness and the structure of the trade-wind layer. *Journal of Advances in Modeling Earth Systems*, 7(4):1741–1764, 2015. ISSN 1942-2466. doi: 10.1002/2015MS000483. URL <http://dx.doi.org/10.1002/2015MS000483>.
- Ole Peters, J. David Neelin, and Stephen W. Nesbitt. Mesoscale convective systems and critical clusters. *Journal of the Atmospheric Sciences*, 66(9):2913–2924, 2009. doi: 10.1175/2008JAS2761.1. URL <http://dx.doi.org/10.1175/2008JAS2761.1>.
- Steven Platnick, Michael D. King, Steven A. Ackerman, W. Paul Menzel, Bryan A. Baum, Jérôme C. Riédi, and Richard A. Frey. The modis cloud products: Algorithms and examples from terra. *IEEE Transactions on Geoscience and Remote Sensing*, pages 459–473, 2003.
- Mirjana Sakradzija and Cathy Hohenegger. What determines the distribution of shallow convective mass flux through cloud base? uploaded on the 16th of May 2017 to AMS, 2017.

- I. Sandu, B. Stevens, and R. Pincus. On the transitions in marine boundary layer cloudiness. *Atmospheric Chemistry and Physics*, 10(5):2377–2391, 2010. doi: 10.5194/acp-10-2377-2010. URL <http://www.atmos-chem-phys.net/10/2377/2010/>.
- David W. Scott. Scott’s rule. *Wiley Interdisciplinary Reviews: Computational Statistics*, 2(4):497–502, 2010. ISSN 1939-0068. doi: 10.1002/wics.103. URL <http://dx.doi.org/10.1002/wics.103>.
- T. H. M. Stein, C. E. Holloway, I. Tobin, and S. Bony. Observed relationships between cloud vertical structure and convective aggregation over tropical ocean. *Journal of Climate*, 30(6):2187–2207, 2017. doi: 10.1175/JCLI-D-16-0125.1. URL <http://dx.doi.org/10.1175/JCLI-D-16-0125.1>.
- Bjorn Stevens. Atmospheric moist convection. *Annual Review of Earth and Planetary Sciences*, 33(1):605–643, 2005. doi: 10.1146/annurev.earth.33.092203.122658. URL <https://doi.org/10.1146/annurev.earth.33.092203.122658>.
- Bjorn Stevens, Helene Brogniez, Christoph Kiemle, Jean-Lionel Lacour, Cyril Crevoisier, and Johannes Killian. Structure and dynamical influence of water vapor in the lower tropical troposphere. submitted, 2017.
- Kurtis J. Thome, Stuart F. Biggar, and Philip N. Slater. Effects of assumed solar spectral irradiance on intercomparisons of earth-observing sensors, 2001. URL <http://dx.doi.org/10.1117/12.450668>.
- Isabelle Tobin, Sandrine Bony, and Remy Roca. Observational evidence for relationships between the degree of aggregation of deep convection, water vapor, surface fluxes, and radiation. *Journal of Climate*, 25(20):6885–6904, 2012. doi: 10.1175/JCLI-D-11-00258.1. URL <http://dx.doi.org/10.1175/JCLI-D-11-00258.1>.
- Panu Trivej and Bjorn Stevens. The echo size distribution of precipitating shallow cumuli. *Journal of the Atmospheric Sciences*, 67(3):788–804, 2010. doi: 10.1175/2009JAS3178.1. URL <http://dx.doi.org/10.1175/2009JAS3178.1>.
- Raphaella Vogel, Louise Nuijens, and Bjorn Stevens. The role of precipitation and spatial organization in the response of trade-wind clouds to warming. *Journal of Advances in Modeling Earth Systems*, 8(2):843–862, 2016. ISSN 1942-2466. doi: 10.1002/2015MS000568. URL <http://dx.doi.org/10.1002/2015MS000568>.
- F. Werner, G. Wind, Z. Zhang, S. Platnick, L. Di Girolamo, G. Zhao, N. Amarasinghe, and K. Meyer. Marine boundary layer cloud property retrievals from highresolution aster observations: Case studies and comparison with teramodis. *Atmospheric Measurement Techniques Discussions*, 2016:1–47, 2016. doi: 10.5194/amt-2016-265. URL <http://www.atmos-meas-tech-discuss.net/amt-2016-265/>.

- Bruce A. Wielicki and Ronald M. Welch. Cumulus cloud properties derived using landsat satellite data. *Journal of Climate and Applied Meteorology*, 25(3):261–276, 1986. doi: 10.1175/1520-0450(1986)025<0261:CCPDUL>2.0.CO;2. URL [http://dx.doi.org/10.1175/1520-0450\(1986\)025<0261:CCPDUL>2.0.CO;2](http://dx.doi.org/10.1175/1520-0450(1986)025<0261:CCPDUL>2.0.CO;2).
- Robert Wood and Christopher S. Bretherton. On the relationship between stratiform low cloud cover and lower-tropospheric stability. *Journal of Climate*, 19(24):6425–6432, 2006. doi: 10.1175/JCLI3988.1. URL <http://dx.doi.org/10.1175/JCLI3988.1>.
- Y. Yamaguchi, A. B. Kahle, H. Tsu, T. Kawakami, and M. Pniel. Overview of advanced spaceborne thermal emission and reflection radiometer (aster). *IEEE Transactions on Geoscience and Remote Sensing*, 36(4):1062–1071, Jul 1998. ISSN 0196-2892. doi: 10.1109/36.700991.
- Guangyu Zhao and Larry Di Girolamo. Statistics on the macrophysical properties of trade wind cumuli over the tropical western atlantic. *Journal of Geophysical Research: Atmospheres*, 112(D10):n/a–n/a, 2007. ISSN 2156-2202. doi: 10.1029/2006JD007371. URL <http://dx.doi.org/10.1029/2006JD007371>. D10204.

## Acknowledgements

I would like to thank my supervisors Prof. Dr. Stefan Bühler and Dr. Ákos Horváth for the many useful discussions and advice on satellite datasets, cloud masking algorithms and suitable variables related to cloud field properties. Thanks for providing such an open and welcoming working atmosphere. I am especially grateful for the comprehensive technical support from Oliver Lemke and Lukas Kluft. Thank you so much for teaching me how to write clean and efficient python scripts.

The ASTER L1B and the MODIS data products were retrieved from the online Data Pool, courtesy of the NASA Land Processes Distributed Active Archive Center (LP DAAC), USGS/Earth Resources Observation and Science (EROS) Center, Sioux Falls, South Dakota, [https://lpdaac.usgs.gov/data\\_access/data\\_pool](https://lpdaac.usgs.gov/data_access/data_pool). I acknowledge ECMWF and the Copernicus Climate Change Service for providing access to the ERA-interim dataset through their public data portal.

I wish to thank Chris Bretherton, Mirjana Sakradzija and Matthias Brück for those intensive discussions on the confusing relations between cloud field properties and other meteorological parameters. I accomplished a better understanding of processes acting in the trades and, most interesting to me, how atmospheric models see the world. Many many thanks to Verena Grützun, Anne, Karo and Reimar for proofreading parts of this thesis. I appreciate all your comments on misleading expressions, typos and those encouraging comments in between. Finally, I wish to thank Morten, Elina, friends and family for supporting me throughout the last months and for listening patiently to my general concerns as well as detailed technical explanations.

## **Versicherung an Eides statt**

Ich versichere an Eides statt, dass ich die vorliegende Arbeit im Studiengang Master of Science Meteorologie selbstständig verfasst und keine anderen als die angegebenen Hilfsmittel — insbesondere keine im Quellenverzeichnis nicht benannten Internet-Quellen — benutzt habe. Alle Stellen, die wörtlich oder sinngemäß aus Veröffentlichungen entnommen wurden, sind als solche kenntlich gemacht. Ich versichere weiterhin, dass ich die Arbeit vorher nicht in einem anderen Prüfungsverfahren eingereicht habe und die eingereichte schriftliche Fassung der auf dem elektronischen Speichermedium entspricht.

Hamburg, den 18. Juni 2017

Theresa Mieslinger